CrossMark

Machine-learning-based feedback control for drag reduction in a turbulent channel flow

Jonghwan Park[1] **and Haecheon Choi**[1,2,†]

[1]Department of Mechanical Engineering, Seoul National University, Seoul 08826, Korea

[2]Institute of Advanced Machines and Design, Seoul National University, Seoul 08826, Korea

One of the successful feedback controls for skin-friction drag reduction designed by Choi *et al.* (*J. Fluid Mech.*, vol. 262, 1994, pp. 75–110), called 'opposition control', has a limitation in application because the sensors need to be placed slightly away from the wall, i.e. at $y^+ = 10$, and measure the instantaneous wall-normal velocity. In the present study we train convolutional neural networks using the database of uncontrolled turbulent channel flow at $Re_\tau = 178$ to extract the spatial distributions of the wall shear stresses and pressure that closely represent the wall-normal velocity at $y^+ = 10$. The correlations between the predicted wall-normal velocities at $y^+ = 10$ from the wall-variable distributions and true ones are very high, and they are 0.92, 0.96 and 0.96 for the streamwise and spanwise wall shear stresses and pressure, respectively. We perform feedback controls of turbulent channel flow with instantaneous blowing and suction determined by the trained convolutional neural networks from the measured wall-variable distributions. The predicted wall-normal velocities during the controls have higher energy at small to intermediate scales than the true ones, which degrades the control performance in skin-friction drag reduction. By applying a low-pass filter to the predicted wall-normal velocities to remove those scales, we reduce skin-friction drag by up to 18 % whose amount is comparable to that by opposition control. The convolutional neural networks trained at $Re_\tau = 178$ are also applied to a higher Reynolds number flow ($Re_\tau = 578$), and provide a successful skin-friction drag reduction of 15 %.

Key words: drag reduction

1. Introduction

A feedback control method for skin-friction drag reduction by Choi, Moin & Kim (1994), called opposition control, is a physics-based control strategy that mitigates the strength of near-wall streamwise vortices in a channel by providing blowing and suction at the wall (ϕ) which is 180° out-of-phase with the instantaneous wall-normal velocity v above the wall. Choi *et al.* (1994) showed that the sensing-plane location of $y^+ \approx 10$ (i.e. $\phi = -v_{y^+ \approx 10}$) was the optimal location providing 25 % skin-friction drag reduction in a turbulent channel flow, where $y^+ = yu_\tau/\nu$, y is the wall-normal distance from the wall, u_τ is the wall shear velocity and ν is the kinematic viscosity. Later, a number of studies have investigated the detailed characteristics of opposition control.

† Email address for correspondence: choi@snu.ac.kr

Hammond, Bewley & Moin (1998) showed that the sensing-plane location of $y^+ = 15$ provided slightly more drag reduction than that of $y^+ = 10$. Chung & Talha (2011) reported that the maximum drag-reduction rate with a given sensing location depended on the amplitude of blowing/suction. For example, approximately 10 % drag reduction was obtained with $\phi = -(v_{y^+=25}/5)$, whereas the drag increased with $\phi = -v_{y^+=25}$. The effect of the Reynolds number had been also investigated; the maximum drag-reduction rate decreased as the Reynolds number increased (Chang, Collis & Ramakrishnan 2002; Iwamoto, Suzuki & Kasagi 2002), but drag reduction of 20 % was still achieved at $Re_\tau = 1000$ with a sensing location of $y^+ = 13.5$ (Wang, Huang & Xu 2016), where $Re_\tau = u_\tau \delta / \nu$ and δ is the channel half-height. Rebbeck & Choi (2001, 2006) experimentally conducted opposition control with a single pair of sensing probe and actuator, and showed that strong downwash motions near the wall were suppressed by the blowing at the wall.

Since it is difficult and even impractical to measure the instantaneous wall-normal velocity v at $y^+ = 10$ (v_{10} hereafter), opposition controls using predicted v_{10}'s (v_{10}^{pred}'s) from wall variables such as the wall pressure and shear stresses have been searched for. For example, Choi *et al.* (1994) conducted a Taylor series expansion on near-wall wall-normal velocity,

$$v(y) = \frac{1}{2} y^2 \left. \frac{\partial^2 v}{\partial y^2} \right|_w + \cdots, \tag{1.1}$$

where $y = 0$ is the wall location and the subscript w denotes the wall. Due to the continuity $(\partial v / \partial y = -\partial u / \partial x - \partial w / \partial z)$,

$$v(y) = -\frac{1}{2} y^2 \left[\frac{\partial}{\partial x} \left. \frac{\partial u}{\partial y} \right|_w + \frac{\partial}{\partial z} \left. \frac{\partial w}{\partial y} \right|_w \right] + \cdots, \tag{1.2}$$

where x and z are the streamwise and spanwise directions, respectively, and u and w are the corresponding velocity components. Because the first term in the bracket had a negligible correlation with v_{10},

$$v(y) \approx -\frac{1}{2} y^2 \frac{\partial}{\partial z} \left. \frac{\partial w}{\partial y} \right|_w, \tag{1.3}$$

and they applied

$$\phi = v_{10,rms} \frac{\partial}{\partial z} \left. \frac{\partial w}{\partial y} \right|_w \bigg/ \left(\frac{\partial}{\partial z} \left. \frac{\partial w}{\partial y} \right|_w \right)_{rms}, \tag{1.4}$$

resulting in approximately 6 % drag reduction. The correlation coefficient between v_{10} and v predicted using this Taylor series expansion was $\rho_{v_{10}} \approx 0.75$, which is not low but not high enough to produce a significant amount of drag reduction. Here, the correlation coefficient between v_{10} and ψ is defined as $\rho_{v_{10}} = \langle v_{10}(x, z, t) \psi(x, z, t) \rangle / (v_{10,rms} \psi_{rms})$, where $\langle \ \rangle$ denotes the averaging in the homogeneous directions (x, z) and time, and the subscript *rms* indicates the root-mean square. Bewley & Protas (2004) retained even high-order terms (up to the terms of $O(y^5)$) in the Taylor series expansion, but high-order terms rather degraded the correlation. Several studies have presented methods of predicting the near-wall velocity from the flow variables at the wall or away from the wall using direct numerical simulation (DNS) data. Podvin & Lumley (1998) conducted a proper orthogonal decomposition (POD) to the streamwise and spanwise wall velocity gradients ($\partial u / \partial y|_w$ and $\partial w / \partial y|_w$), and showed that near-wall streamwise streaks were reconstructed well but wall-normal and spanwise velocities were not very well reproduced. Bewley & Protas (2004) developed an adjoint-based estimator which was optimized by

solving the adjoint Navier–Stokes equations. An estimator using all three wall variables ($\partial u/\partial y|_w$, $\partial w/\partial y|_w$ and p_w (wall pressure)) showed a better prediction of near-wall velocity components for a turbulent channel flow at $Re_\tau = 100$ than that from the Taylor series expansion, showing $\rho_{v_{10}} \approx 0.88$. Hœpffner *et al.* (2005) and Chevalier *et al.* (2006) developed a linear estimation model based on the linearized Navier–Stokes equations and a Kalman filter. They improved the performance of the estimator by treating nonlinear terms in the Navier–Stokes equations as the external forcings which were sampled from DNS data, and obtained $\rho_{v_{10}} \approx 0.85$ using three wall variables of $\omega_y|_w$, $\partial^2 v/\partial y^2|_w$, and p_w for a turbulent channel flow at $Re_\tau = 100$, where $\omega_y|_w$ is the wall-normal vorticity at the wall. Illingworth, Monty & Marusic (2018) applied a linear estimator similar to that of Chevalier *et al.* (2006) to a turbulent channel flow at $Re_\tau = 1000$, and predicted large scale u at an arbitrary y location using all three velocity components at $y^+ = 197$. A linear estimator based on $\partial u/\partial y|_w$ also reasonably predicted large scale u at an arbitrary y, but its performance was not better than that using all three velocity components at $y^+ = 400$ in a turbulent channel flow at $Re_\tau = 2000$ (Oehler, Garcia-Gutiérrez & Illingworth 2018). Oehler & Illingworth (2018) used an estimator to impose a body forcing $f_b|_{y=y_b}$ predicted by sensing $u|_{y=y_s}$ or $\partial u/\partial y|_w$, for the minimization of the magnitude of the velocity fluctuations in a turbulent channel flow at $Re_\tau = 2000$, and obtained a minimum value when $y_s = 0.26\delta$ and $y_b = 0.29\delta$.

Another approach for predicting v_{10} with the wall variables is using a neural network. Lee *et al.* (1997) applied a neural network for the first time to perform a control with v_{10}^{pred} (predicted v_{10}) in a turbulent channel flow at $Re_\tau = 100$. They used the information of $\partial w/\partial y|_w$ along the spanwise direction to predict v_{10} (i.e. $v_{10}^{pred}(x, z) = f(\partial w/\partial y|_w(x, z \pm n\Delta z))$, $n = 0, 1, 2, \ldots$), and showed that the spanwise length of at least 90 wall units was required for accurately predicting v_{10} with $\partial w/\partial y|_w$'s, resulting in $\rho_{v_{10}}$ of approximately 0.85 and 18 % drag reduction. Lorang, Podvin & Le Quéré (2008) obtained the first POD mode of v_{10} with a neural network by sensing whole domain information of $\partial w/\partial y|_w$ in a turbulent channel flow at $Re_\tau = 140$, and performed a control with it, resulting in a drag reduction of 13 % which was slightly smaller than the amount of drag reduction (14 %) with the method of Lee *et al.* (1997). The difference in the amounts of drag reduction from those two studies may come from the difference in the Reynolds numbers, i.e. $Re_\tau = 100$ versus 140. Milano & Koumoutsakos (2002) used a neural network to predict high-order terms ($O(y^3)$) of the Taylor series expansion of near-wall velocity components by sensing p_w, $\partial u/\partial y|_w$ and $\partial w/\partial y|_w$, and the reconstructed streamwise and spanwise velocities had correlations higher than 0.9, but $\rho_{v_{10}}$ (obtained from the continuity) was only approximately 0.6. Recently, Yun & Lee (2017) used p_w to predict v_{10} by a neural network with the streamwise and spanwise sensing lengths of 90 and 45 wall units, respectively, and showed $\rho_{v_{10}} = 0.85$. These previous studies showed that the neural network is an attractive tool to predict v_{10} with wall-variable sensing, but shallow neural networks (one nonlinear layer in Lee *et al.* (1997) and Lorang *et al.* (2008), two nonlinear layers in Milano & Koumoutsakos (2002) and Yun & Lee (2017)) may not be sufficient to yield a high $\rho_{v_{10}}$.

In recent years, machine learning, especially deep learning (LeCun, Bengio & Hinton 2015), has shown remarkable performance. Güemes, Discetti & Ianiro (2019) applied an extended POD and convolutional neural networks, respectively, to reconstruct large- and very large-scale motions in a turbulent channel flow based on the wall shear stress measurement, and showed that the convolutional neural networks performed significantly better than the extended POD. Kim & Lee (2020) used a nine-layer convolutional neural network (CNN) to predict the heat flux at the wall using wall variables (p_w, $\partial u/\partial y|_w$ and

$\partial w/\partial y|_w$), and showed that the CNN outperformed a linear regression. So far, there is no attempt to apply a CNN to the prediction of the near-wall flow (v_{10}) from the flow variables at the wall and to the flow control in a feedback manner. Therefore, in the present study we first aim at predicting v_{10} using a CNN which is currently the most successful deep learning method in discovering spatial distributions of a raw input that are closely related to a desired output, where the wall flow variables (p_w, $\partial u/\partial y|_w$ and $\partial w/\partial y|_w$) and v_{10} are the input and output, respectively, used in this study. We investigate how high $\rho_{v_{10}}$ can be achieved from the CNN as compared to fully connected neural networks (FCNN) used in the previous studies (Lee *et al.* 1997; Milano & Koumoutsakos 2002; Lorang *et al.* 2008; Yun & Lee 2017). We then perform opposition control with v_{10}^{pred} predicted by the CNN. Because the controlled flow is not available in practice, we train our CNN only with the uncontrolled flow. Note that previous studies (Lee *et al.* 1997; Lorang *et al.* 2008) used controlled flows to train the neural network. Finally, we apply the CNN to a higher Reynolds number flow to see if the prediction and control capabilities are maintained even if the CNN is trained with a lower Reynolds number flow. Details of the problem setting, CNN, and numerical method are presented in § 2. The prediction performance of the CNN is given in § 3. In § 4 we provide the results of control with v_{10}^{pred} from the CNN. An application to a higher Reynolds number flow is given in § 5, followed by conclusions. In the appendices the results from other machine learning techniques such as the random forest and FCNN are given and their results are briefly discussed.

2. Methodology

2.1. *Problem setting*

In the present study we predict v_{10} from a spatial distribution of wall variables (χ_w) in a turbulent channel flow, where a CNN is used to extract hidden features of χ_w which may closely represent v_{10}. We consider three different wall variables ($\chi_w = p_w$, $\partial u/\partial y|_w$ and $\partial w/\partial y|_w$) that are measurable quantities in real systems (Kasagi, Suzuki & Fukagata 2008). Each of these wall variables is used to predict v_{10} (figure 1) and is used for the control. Since Bewley & Protas (2004) and Chevalier *et al.* (2006) showed that using more wall variables improved the prediction performance, all three wall variables are also used to predict v_{10} and the results are given in § 4.3. A region on the wall (coloured in yellow) in figure 1 is an example of the sensing region of the wall variable χ_w whose streamwise and spanwise lengths are approximately 90 wall units. The size of each sensing region is selected considering those of previous studies in which at least 90 wall units in the spanwise direction was required for $\partial w/\partial y|_w$ (Lee *et al.* 1997), and 90 wall units in the streamwise direction was sufficient for p_w (Yun & Lee 2017). One of the wall variables is the input of the present CNN (see below), and the output is v_{10}^{pred} at the centre location of each sensing region. As we show below, this size is not big enough to include the influence of v_{10} on the wall variables, but is still sufficient to have a high correlation between v_{10} and v_{10}^{pred}.

The two-point correlation coefficient ρ between v_{10} and χ_w in a turbulent channel flow is defined as

$$\rho\,(\Delta x,\,\Delta z) = \frac{\langle v_{10}(x, z, t)\chi_w(x + \Delta x, z + \Delta z, t)\rangle}{v_{10,rms}\chi_{w,rms}}, \tag{2.1}$$

where $\langle v_{10}\rangle = 0$, and Δx and Δz are the separation distances in the streamwise and spanwise directions, respectively. Figure 2 shows the contours of the two-point correlations for three different flows: (*a–c*) uncontrolled flow at $Re_\tau = 178$, (*d–f*) controlled flow
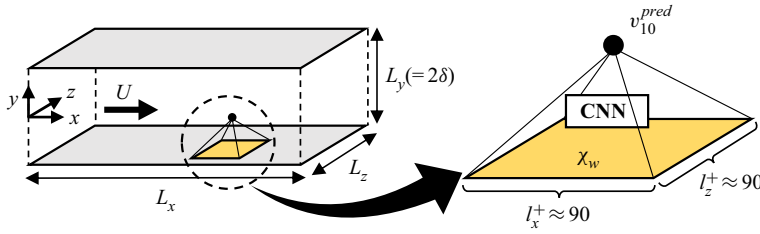
FIGURE 1. Schematic diagram on the relation between the predicted v at $y^+ = 10$ (v_{10}^{pred}) and wall-variable distribution with a CNN in a turbulent channel flow. The input (χ_w) of the CNN is one of p_w, $\partial u/\partial y|_w$ and $\partial w/\partial y|_w$, and the output is v_{10}^{pred}.

with opposition control (Choi *et al.* 1994) at $Re_\tau = 178$, and (*g–i*) uncontrolled flow at $Re_\tau = 578$, where $Re_\tau = u_{\tau_o}\delta/\nu$ and u_{τ_o} is the wall shear velocity of the uncontrolled flow. These correlation contours indicate that there are distinct regions of close relations between v_{10} and χ_w. For the uncontrolled flow at $Re_\tau = 178$ (figure 2*a–c*), the wall pressure has the highest correlation on the downstream of v_{10}, but has the lowest maximum correlation among three wall variables investigated in this study. The streamwise wall shear rate $\partial u/\partial y|_w$ has the highest correlation at the upstream of v_{10}, whereas the correlation with the spanwise wall shear rate $\partial w/\partial y|_w$ is highest at slightly downstream but sideways locations. The two-point correlation is highest for the spanwise wall shear rate, but this correlation magnitude ($\rho = 0.56$) is not high enough to accurately predict v_{10}. Also, these correlation contours themselves do not provide how one can construct v_{10} from this information. Hence, in the present study, we construct v_{10} from the wall-variable information in $-45 < \Delta x^+ < 45$ and $-45 < \Delta z^+ < 45$ using a CNN, and discuss how high correlations can be obtained from this approach.

For the controlled flow at $Re_\tau = 178$ (figure 2*d–f*), the correlations with p_w and $\partial w/\partial y|_w$ are very similar to those for the uncontrolled flow. This suggests that a CNN trained with the uncontrolled flow can be applied to predict v_{10} for the controlled flow and also to control the flow in a feedback manner even without requiring training data of the controlled flow. On the other hand, the correlations with $\partial u/\partial y|_w$ have opposite signs in many places to those for the uncontrolled flow. This is because the blowing and suction at the wall from opposition control changes $\partial u/\partial y|_w$ to be approximately $180°$ out-of-phase different from v_{10}. For the uncontrolled flow at $Re_\tau = 578$ (figure 2*g–i*), the correlations are very similar to those at $Re_\tau = 178$, as the near-wall flow is well scaled in wall units, which suggests that the CNN trained at a lower Reynolds number should be applicable to the flow at a higher Reynolds number.

Note that near-wall flow structures are significantly changed by opposition control (Choi *et al.* 1994; Hammond *et al.* 1998), and a higher Reynolds number flow contains smaller scales than those at $Re_\tau = 178$. Therefore, the success of the present control based on a CNN trained with uncontrolled flow at $Re_\tau = 178$ relies on the proper selection of wall sensing variable that maintains a similar correlation coefficient with v_{10} for controlled and higher Reynolds number flows. For the present turbulent channel flow, the wall sensing variables satisfying this requirement are p_w and $\partial w/\partial y|_w$, but $\partial u/\partial y|_w$ fails to satisfy this requirement. The details of the CNN used are provided in § 2.3. Other machine learning techniques such as the Lasso, random forest and FCNN are also tested, and comparisons of the prediction performance by different machine learning techniques are given in appendix A.
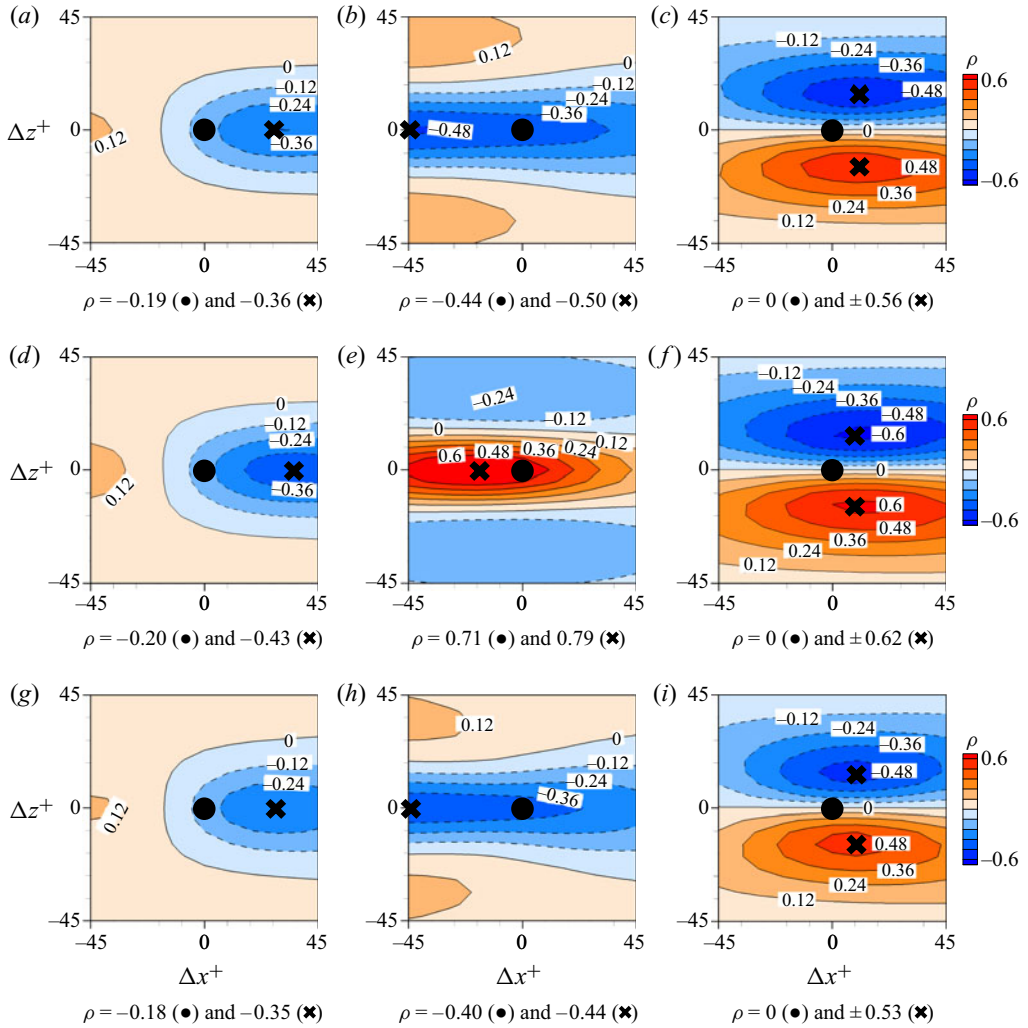
FIGURE 2. Contours of the correlation coefficients between v_{10} and χ_w: $(a–c)$ uncontrolled flow at $Re_\tau = 178$; $(d–f)$ controlled flow at $Re_\tau = 178$ by opposition control; $(g–i)$ uncontrolled flow at $Re_\tau = 578$. (a,d,g) $\chi_w = p_w$, (b,e,h) $\chi_w = \partial u/\partial y|_w$ and (c,f,i) $\chi_w = \partial w/\partial y|_w$. Solid circles at the centre denote the location of v_{10} ($\Delta x = \Delta z = 0$), and cross symbols are the locations of the maximum correlation magnitude. The values of ρ at these locations are given at the bottom of each figure. Here, $\Delta x^+ = \Delta x u_{\tau_o}/v$ and $\Delta z^+ = \Delta z u_{\tau_o}/v$.

2.2. *The dataset*

The dataset (v_{10}^{true}, χ_w) for training a CNN is obtained from direct numerical simulation of a turbulent channel flow at $Re_\tau = 178$, where $v_{10}^{true} = v_{10}$. The governing equations for the continuity and incompressible Navier–Stokes equations are

$$\frac{\partial u_i}{\partial x_i} = 0, \tag{2.2}$$

$$\frac{\partial u_i}{\partial t} + \frac{\partial u_i u_j}{\partial x_j} = -\frac{\mathrm{d}P}{\mathrm{d}x_1}\delta_{1i} - \frac{\partial p}{\partial x_i} + \frac{1}{Re}\frac{\partial^2 u_i}{\partial x_j \partial x_j}, \tag{2.3}$$

where $x_i (= (x, y, z))$ are the Cartesian coordinates, $u_i (= (u, v, w))$ are the corresponding velocity components, p is the pressure fluctuation, $-dP/dx_1$ is the mean pressure gradient to maintain a constant mass flow rate in a channel. The Reynolds number is $Re = 5600$ based on the bulk velocity (u_b) and channel height (2δ), and is 178 based on the wall shear velocity of the uncontrolled flow (u_{τ_o}) and channel half-height (δ). A semi-implicit fractional step method is used to solve (2.2) and (2.3), where a third-order Runge–Kutta and the Crank–Nicolson schemes are used for the convection and diffusion terms, respectively. For spatial derivatives, the second-order central difference scheme is used. The no-slip condition is applied to the upper and lower walls, and periodic boundary conditions are used in the wall-parallel directions. The computational domain size is $3\pi\delta(x) \times 2\delta(y) \times \pi\delta(z)$ and the number of grid points is $192(x) \times 129(y) \times 128(z)$. In the wall-normal direction a non-uniform grid is used with $\Delta y^+ \approx 0.2 - 7.0$ (dense grids near the wall). Uniform grids are used in the wall-parallel directions with $\Delta x^+ \approx 8.7$ and $\Delta z^+ \approx 4.4$.

The simulation starts with a laminar velocity profile with random perturbations and continues until the flow reaches a fully developed state. Then, 740 instantaneous fields of v_{10}^{true} and χ_w's ($= p_w$, $\partial u/\partial y|_w$, and $\partial w/\partial y|_w$) are stored during $T^+ = Tu_{\tau_o}^2/\nu = 29\,560$ with an interval of $\Delta T^+ = 40$, where v_{10}^{true} is the label for output of a CNN (v_{10}^{pred}), and χ_w's are the input whose domain size is approximately $90(l_x^+) \times 90(l_z^+)$ in wall units (corresponding to 11×21 grid points, respectively), as shown in figure 1. Here, one instantaneous field contains the information of χ_w's and v_{10}^{true} at both sides of the channel. The χ_w and v_{10}^{true} are normalized with their root-mean-square (subscript *rms*) values as

$$\chi_w^* = \frac{\chi_w - \langle \chi_w \rangle}{\chi_{w,rms}}, \quad v_{10}^* = \frac{v_{10}^{true}}{v_{10,rms}^{true}}, \quad (2.4a,b)$$

where $\langle \chi_w \rangle$ denotes the mean value of χ_w. The dataset of χ_w^* and v_{10}^* is divided into three sets of different sizes, i.e. training, validation and test sets. Only the training set is used for optimizing a CNN. The validation set is used for checking the optimization process at each training iteration, and the prediction performance is evaluated with the test set after the whole training procedure is finished. We use 700 instantaneous fields (containing 34 406 400 pairs of χ_w's and v_{10}^{true}) for the training, and extract data at every third grid point in the streamwise and spanwise directions (resulting in approximately 3.8 million pairs of χ_w's and v_{10}^{true}), respectively, to exclude highly correlated data. Twenty instantaneous fields (containing 983,040 pairs of χ_w's and v_{10}^{true}) are used for each validation and test set. Here, we use the number of training data of $N_{train} \approx 3.8 \times 10^6$ which is approximately three times that used in the ImageNet large-scale visual recognition challenge (ILSVRC) for developing convolutional neural networks (Krizhevsky, Sutskever & Hinton 2012; Simonyan & Zisserman 2014; Szegedy *et al.* 2014; He *et al.* 2015; Russakovsky *et al.* 2015). This is because the present training searches for the spatial correlations of χ_w's and v_{10}^{true} and, thus, it possesses some similarity with that of image recognition in the ILSVRC, but it may require more training data due to the unsteady characteristics of the present problem than that used in the ILSVRC. In appendix B we show that $N_{train} \approx 3.8 \times 10^6$ is sufficient for the present problem.

2.3. *Convolutional neural network*

The CNN is a class of neural network, composed of input, hidden and output layers with artificial neurones. The CNN uses a discrete convolution operation with filters to construct the next layer keeping spatially two-dimensional feature maps. Therefore, unlike a FCNN
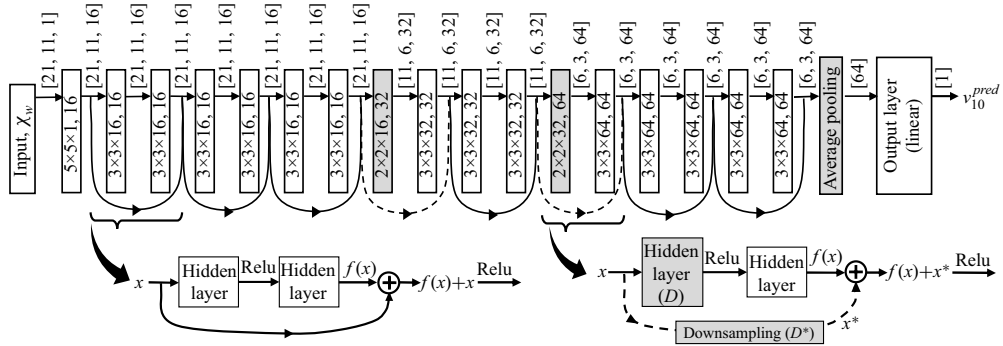
FIGURE 3. Architecture of the CNN used in the present study. Each box and arrow after the input and before the average pooling layer represent a hidden layer and flow of the feature maps, respectively. Dimensions of the feature maps, denoted as [height (h_m), width (w_m), depth (d_m)], are given next to the arrows, and the size and number of filters ($h_f \times w_f \times d_{input}$, d_{output}, respectively) are given inside each box. The h_m and w_m are the numbers of grid points of the feature maps in the z and x directions, respectively. The h_f and w_f are the numbers of filter weights in the z and x directions, respectively. Zero paddings are used to adjust the sizes of h_m and w_m of the feature maps after convolution operations. Grey-coloured boxes are the downsampling layers. A residual block without a downsampling layer (lower left figure) consists of two hidden layers, and its output is the sum of the output from the last hidden layer $f(x)$ and the input of the residual block x. For a residual block with a downsampling layer (lower right figure), its output is the sum of the output from the last hidden layer $f(x)$ and the downsampled input x^*, where downsampling (D^*) is carried out with the same filter size and stride as those of the downsampling layer (D). For downsampling (D and D^*), zero padding is applied on the bottom row or right column of a feature map when h_m or w_m of the input x is an odd number.

whose inputs to a neurone are outputs from all neurones in the previous layer, local outputs from the previous layer in the CNN are inputs to a neurone, and neurones share the same weights (LeCun *et al.* 1989, 2015). Figure 3 shows the architecture of the CNN used in the present study. We use 17 hidden layers, one average pooling layer and one linear layer adopting a residual block proposed by He *et al.* (2015). For the hidden layers without downsampling, we use a filter size of 3×3 or 5×5, with a stride of 1 for the convolution, where the stride is the magnitude of movement between applications of the filter to the input feature map (Singh & Manure 2019). After the first and second downsampling layers, the height (h_m) and width (w_m) of the feature maps are reduced by half, and the depth (d_m) is doubled, as in He *et al.* (2015). We use a convolution operation with a stride of 2 and a filter size of 2×2 for the first and second downsampling layers. After h_m or w_m of the feature map becomes equal to h_f or w_f of the filter, respectively, we use global average pooling for the last downsampling (average pooling layer in figure 3), where the feature map is averaged while keeping the depth unchanged. After the average pooling layer, the feature map is connected to the linear layer to print out v_{10}^{pred} without an activation function. In the present CNN Relu (Nair & Hinton 2010) is used as the activation function, and a batch normalization (Ioffe & Szegedy 2015) is applied after each convolution operation. All weights (w_j) in the filters are initialized by the Xavier method (Glorot & Bengio 2010), and they are optimized to minimize a given loss function defined as

$$L = \frac{1}{2N} \sum_{i=1}^{N} \left(\frac{v_{10\,i}^{pred} - v_{10\,i}^{true}}{v_{10,rms}^{true}} \right)^2 + 0.025 \sum_j w_j^2, \qquad (2.5)$$

where N is the number of mini-batch data (256 in this study following He *et al.* 2015). An adaptive moment estimation (Kingma & Ba 2014), which is a variant of gradient descent, is used for updating the weights, and the gradients of the loss function with respect to the weights are calculated through the back-propagation algorithm (Rumelhart, Hinton & Williams 1986). We conduct early stopping to prevent overfitting (Bengio 2012). There are many user-defined parameters in constructing a CNN. A study on these parameters is conducted and its results are given in appendix B.

3. Prediction performance

In this section we estimate the performance of the CNN in predicting v_{10}^{true} with χ_w's by analysing the instantaneous and statistical quantities of v_{10}^{pred}'s.

3.1. *Multiple input (spatial distribution of χ_w) and single output (v_{10}^{pred} at a point)*

The correlation coefficients between v_{10}^{true} and v_{10}^{pred}'s by the CNN with $\chi_w = p_w$, $\partial u/\partial y|_w$ and $\partial w/\partial y|_w$ are $\rho_{v_{10}} = 0.95$, 0.90 and 0.95, respectively, where $\rho_{v_{10}} = \langle v_{10}^{true}(x, z, t) v_{10}^{pred}(x, z, t) \rangle / (v_{10,rms}^{true} v_{10,rms}^{pred})$. These magnitudes are much bigger than the maximum two-point correlations described before ($\rho = 0.36$, 0.50 and 0.56, respectively) and also those from other machine learning techniques considered (appendix A). Figure 4 shows the instantaneous fields of v_{10}^{true} and v_{10}^{pred}'s reconstructed by the CNN, together with χ_w's. Although the distributions of χ_w's are very different from that of v_{10}^{true}, the CNN captures most of the v_{10} field from all the wall variables investigated, indicating that the CNN is an adequate tool to predict v_{10}. To understand how v_{10}^{pred} is correlated with χ_w, we compute the saliency map proposed by Simonyan, Vedaldi & Zisserman (2013), and provide the results in appendix C.

3.2. *Multiple input and multiple output (spatial distributions of χ_w and v_{10}^{pred})*

Although the CNN in § 3.1 performed well, the reconstructed flow field v_{10}^{pred} (figure 4) contained spatial oscillations that might provide numerical instability during feedback control. To understand the source of these oscillations, we (i) try even numbers of grid points (24×12) for χ_w to see if they came from zero paddings at the downsampling layers owing to the use of odd numbers (21×11); (ii) use a continuous activation function, $y = \tanh(x)$, since we used a discontinuous activation function (Relu), $y = \max(0, x)$; (iii) apply a linear regression model (Lasso) with 21×11 grid points for χ_w. The spatial oscillations in v_{10}^{pred} still exist for (i) and (ii), but disappear for (iii) (not shown in this paper). This may indicate that the spatial oscillations in v_{10}^{pred} occur because it is nonlinearly determined with χ_w by the CNN. Therefore, to obtain a smoother distribution of v_{10}^{pred} in space, we consider another CNN in this section in which multiple output (a spatial distribution of v_{10}^{pred}) is produced from multiple input (a spatial distribution of χ_w). We call this CNN an MP-CNN, whereas the CNN in § 3.1 is called 1P-CNN.

Figure 5 shows the schematic diagrams of 1P-CNN and MP-CNN. For MP-CNN, we keep the architectures of all hidden layers of 1P-CNN (17 hidden layers), and then add three additional hidden layers. The sizes of the input wall variable χ_w and output v_{10}^{pred} are $l_x^+ \times l_z^+ \approx 270 \times 135$ and 130×65, respectively, and the corresponding numbers of grid points for the input and output are 32×32 and 16×16, respectively. The centre positions of the input and output are the same. The input size in space should be taken to
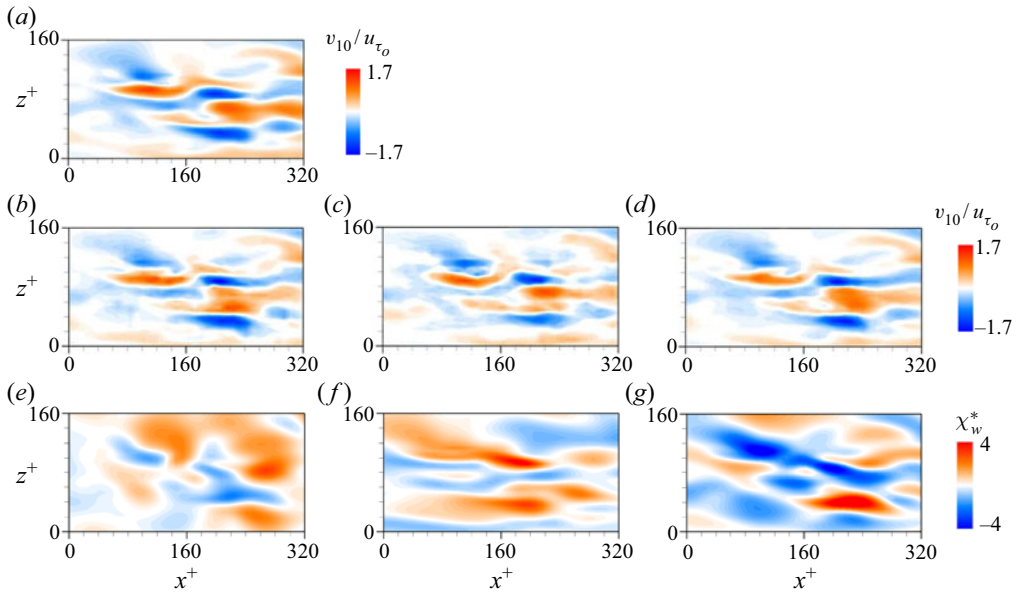
FIGURE 4. Contours of the instantaneous v_{10}^{true}, v_{10}^{pred}'s and instantaneous χ_w's: (a) v_{10}^{true} (DNS); (b) v_{10}^{pred} from $\chi_w = p_w$; (c) v_{10}^{pred} from $\chi_w = \partial u/\partial y|_w$; (d) v_{10}^{pred} from $\chi_w = \partial w/\partial y|_w$; (e) p_w; (f) $\partial u/\partial y|_w$; (g) $\partial w/\partial y|_w$.

be larger than the output size, because v_{10} at a point is correlated with the wall variables nearby. As shown in figure 2, the maximum correlations between v_{10} and χ_w's occur at $|\Delta x^+| \leq 45$ and $|\Delta z^+| \leq 15$, and, thus, the input size, which is twice the output size, should be enough to produce high performance of MP-CNN. The choice of the output size, $l_x^+ \times l_z^+ \approx 130 \times 65$, is rather arbitrary, but this size is at least comparable to the size of a region of rapidly varying v_{10} (see, for example, figure 4). A dataset of χ_w and v_{10}^{true} are obtained from direct numerical simulation of a turbulent channel flow as before. We apply the generative adversarial networks (GAN; Goodfellow *et al.* 2014) to optimize MP-CNN, because previous studies (Ledig *et al.* 2016; Lee & You 2019) showed that a CNN trained with GAN produces more realistic images than using only the quadratic error as a loss function. The details about GAN and loss function are described in appendix D.

Figure 6 shows v_{10}, $\partial v_{10}/\partial x$ and $\partial v_{10}/\partial z$ from 1P-CNN and MP-CNN with $\chi_w = \partial u/\partial y|_w$, respectively, together with those from DNS. The correlation coefficients between the true (DNS) and predicted values with MP-CNN are $\rho = 0.92$, 0.87 and 0.91 for v_{10}, $\partial v_{10}/\partial x$ and $\partial v_{10}/\partial z$, respectively, whereas those with 1P-CNN are $\rho = 0.90$, 0.81 and 0.89, respectively. The results of the correlation coefficients and reconstructed fields (figure 6) indicate that the prediction performance is improved both quantitatively and qualitatively with MP-CNN. Note that oscillations observed with 1P-CNN nearly disappear with MP-CNN. For $\chi_w = p_w$, the correlation coefficients for v_{10}, $\partial v_{10}/\partial x$ and $\partial v_{10}/\partial z$ are $\rho = 0.96$, 0.92 and 0.96 with MP-CNN, respectively, whereas those with 1P-CNN are $\rho = 0.95$, 0.89 and 0.95, respectively. For $\chi_w = \partial w/\partial y|_w$, $\rho = 0.96$, 0.90 and 0.96 with MP-CNN, whereas $\rho = 0.95$, 0.89 and 0.95 with 1P-CNN. The reconstructions with $\chi_w = p_w$ and $\partial w/\partial y|_w$ show results similar to those with $\chi_w = \partial u/\partial y|_w$.

Figure 7 shows the streamwise and spanwise energy spectra of v_{10}^{pred} from $\chi_w = p_w$, $\partial u/\partial y|_w$ and $\partial w/\partial y|_w$, together with those of v_{10}^{true}. Overall, both 1P-CNN and MP-CNN
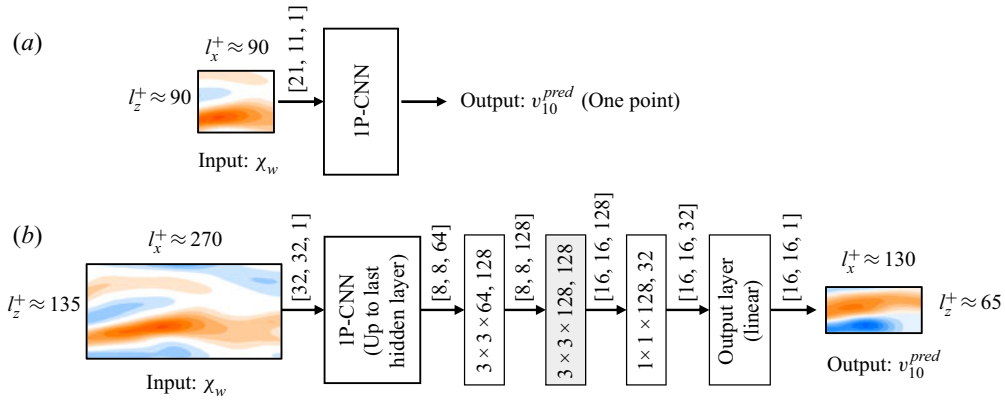
FIGURE 5. Schematics of the present convolutional neural networks: (*a*) 1P-CNN; (*b*) MP-CNN. The detail of 1P-CNN is given in figure 3. For MP-CNN, the size and number of filters are given in each box, and the dimensions of the feature maps are given next to each arrow. The grey-coloured box is the deconvolution layer where the height and width of the feature map increase twice.
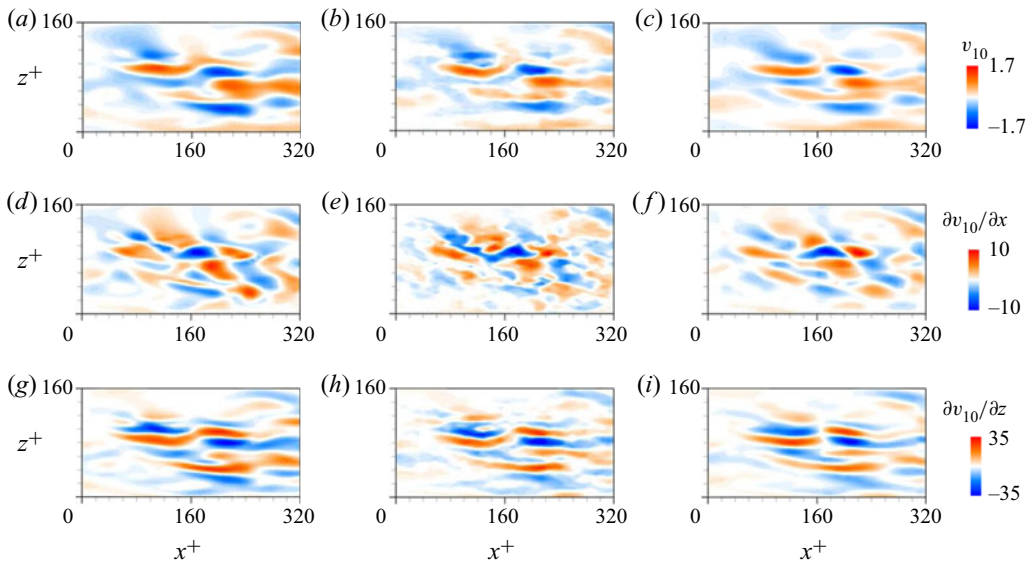

FIGURE 6. Contours of the instantaneous v_{10}, $\partial v_{10}/\partial x$ and $\partial v_{10}/\partial z$: (*a–c*) v_{10}; (*d–f*) $\partial v_{10}/\partial x$; (*g–i*) $\partial v_{10}/\partial z$. (*a,d,g*) are from DNS, and (*b,e,h*) and (*c,f,i*) are from 1P-CNN and MP-CNN with $\chi_w = \partial u/\partial y|_w$, respectively. Here, $\partial v_{10}/\partial x$ and $\partial v_{10}/\partial z$ are calculated using the second-order central difference. Flow variables are normalized with u_{τ_o} and δ.

predict the energy spectra very well. At high wavenumbers, 1P-CNN exhibits severe energy pile up both in the streamwise and spanwise wavenumbers, whereas MP-CNN reduces the energy pile up in the streamwise wavenumber and matches the spanwise energy spectrum nearly perfectly at all wavenumbers. This indicates that small-scale motions of v_{10} is better predicted by MP-CNN than by 1P-CNN.
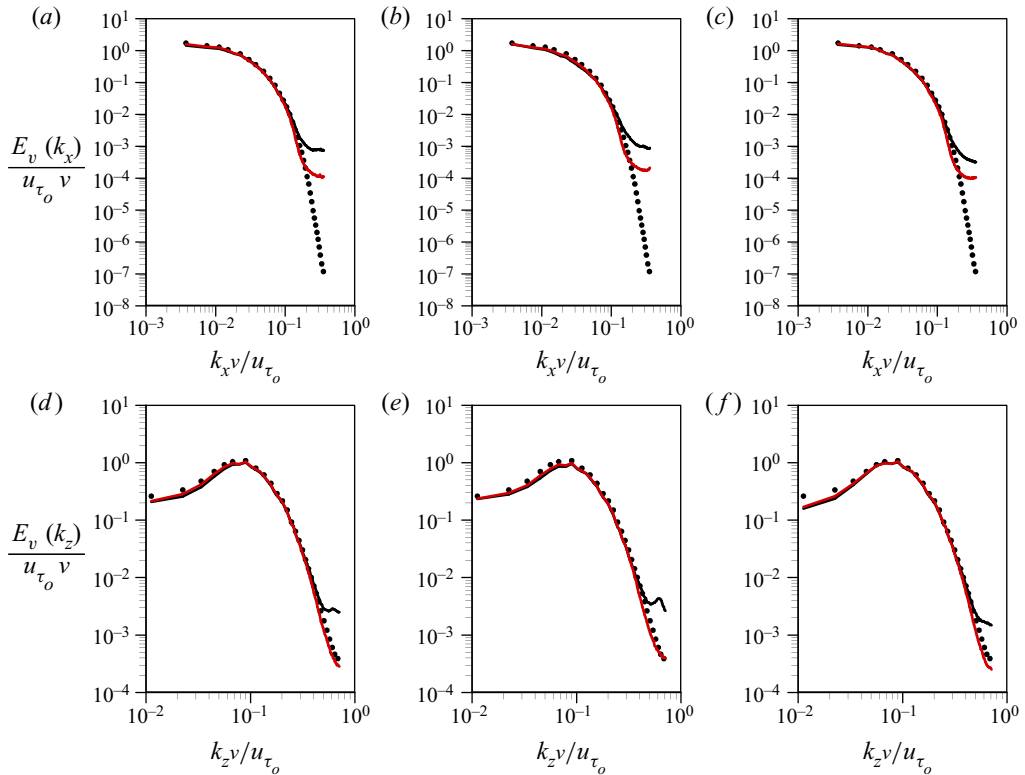
FIGURE 7. Energy spectra of v_{10} from $\chi_w = p_w$, $\partial u/\partial y|_w$, and $\partial w/\partial y|_w$ (uncontrolled flow): (*a–c*) streamwise wavenumber; (*d–f*) spanwise wavenumber. (*a, d*) $\chi_w = p_w$; (*b, e*) $\chi_w = \partial u/\partial y|_w$; (*c, f*) $\chi_w = \partial w/\partial y|_w$. Black circle, v_{10}^{true} (DNS); black line, v_{10}^{pred} with 1P-CNN; red line, v_{10}^{pred} with MP-CNN.

An additional advantage of MP-CNN is a significant reduction of the computational cost. Total of $192(x) \times 128(z)$ prediction processes should be required to reconstruct an entire v_{10} field with 1P-CNN, where one prediction process means one operation of the CNN to print out v_{10}^{pred} with given χ_w. Because the number of the grid points of v_{10}^{pred} is $16(x) \times 16(z)$ for MP-CNN, it requires only $192/16(x) \times 128/16(z)$ prediction processes to reconstruct an entire field. Although the computational cost for one prediction process is greater for MP-CNN due to larger input and output sizes than for 1P-CNN, the computational time required to reconstruct the entire field is approximately 40 times smaller with MP-CNN than that with 1P-CNN.

4. Application to feedback control

In this section we apply MP-CNN to opposition control (Choi *et al.* 1994) for skin-friction drag reduction, $v_w(x, z) = -v_{10}^{pred}(x, z)$, where v_{10}^{pred} is obtained from $\chi_w = p_w$, $\partial u/\partial y|_w$, or $\partial w/\partial y|_w$. We train our MP-CNN with the uncontrolled turbulent channel flow because the controlled flow data is not available in practical situations, and we conduct an off-line control in which MP-CNN is not trained during the control. This is different from the approaches taken by the previous studies (Lee *et al.* 1997; Lorang
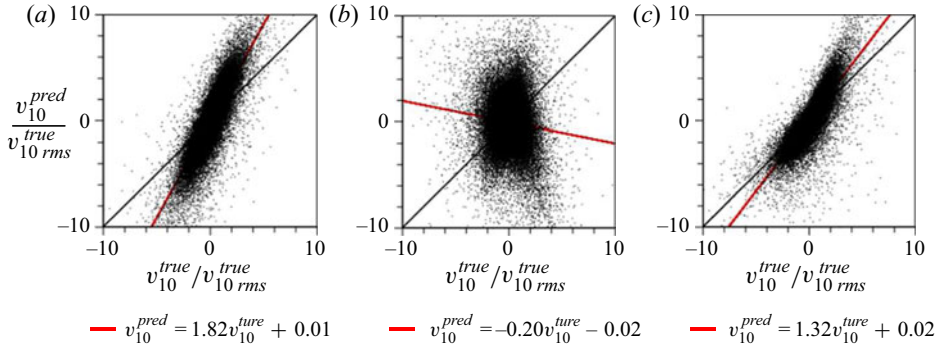
FIGURE 8. Scatter plots of v_{10}^{true} and v_{10}^{pred}: (a) $\chi_w = p_w$; (b) $\chi_w = \partial u/\partial y|_w$; (c) $\chi_w = \partial w/\partial y|_w$. Here, χ_w's and v_{10}^{true} are from the controlled flow with original opposition control (Choi *et al.* 1994), while MP-CNN is trained with the uncontrolled flow. A black line in each figure denotes the slope of 1, and a red line is a fitting line for each scatter plot and is given at the bottom of each figure.

et al. 2008) in which neural networks were trained with the controlled flow data from opposition control. The rationale of using the CNN trained with the uncontrolled flow for the present control was already explained in the discussion related to figure 2. The control input v_w is updated at every 20 computational time steps $\Delta t_c (= 20\Delta t)$, where Δt is the computational time step ($\Delta t^+ = \Delta t u_{\tau_o}^2/\nu = 0.08$). As observed in the previous study (Lee, Kim & Choi 1998), the control performance is not degraded even if Δt_c is greater than Δt, and drag-reduction rate with $\Delta t_c = 20\Delta t$ differs only by 0.5 % compared to that with $\Delta t_c = \Delta t$ in our numerical simulation with opposition control.

4.1. *Control with v_{10}^{pred}*

Figure 8 shows the scatter plots of v_{10}^{true} (from opposition control) and v_{10}^{pred} by MP-CNN trained with the uncontrolled flow. The MP-CNN trained with the uncontrolled flow completely loses its prediction performance for $\chi_w = \partial u/\partial y|_w$ (figure 8b), whereas it still maintains approximately linear relations (but with slopes different from 1) for $\chi_w = p_w$ and $\partial w/\partial y|_w$. Therefore, we modify the magnitude of v_{10}^{pred} at each control time step such that the control becomes

$$v_w = -\sigma v_{10}^{pred} \quad \text{with } \sigma = 0.5 v_{10,rms}^{true}(\text{uncontrolled})/v_{10,rms}^{pred}, \tag{4.1}$$

because $v_{10,rms}^{true}$ (controlled) $\approx 0.5 v_{10,rms}^{true}$ (uncontrolled) under opposition control (Kim & Choi 2017). Instead of using σ in (4.1), the fitting lines given in figure 8 may be used to determine σ. However, as these relations are *a priori* unknown in practical situations, we use a simple relation (4.1) for the control. The correlation coefficients between v_{10}^{true} (controlled) and σv_{10}^{pred}'s from $\chi_w = p_w$, $\partial u/\partial y|_w$ and $\partial w/\partial y|_w$ are $\rho_{v_{10}} = 0.85, -0.08$ and 0.84, respectively, and they are lower than those from the uncontrolled flow (0.96, 0.92 and 0.96, respectively). This is expected because the current MP-CNNs are trained with the uncontrolled flow. Nevertheless, those correlation coefficients for $\chi_w = p_w$ and $\partial w/\partial y|_w$ are high enough to reconstruct v_{10} even for the controlled flow (figure 9). Therefore, we perform a feedback control based on (4.1) and v_{10}^{pred} by MP-CNN trained with the uncontrolled flow. Note that when MP-CNN is trained with the controlled flow, $\rho_{v_{10}} = 0.97, 0.98$ and 0.98 for $\chi_w = p_w$, $\partial u/\partial y|_w$ and $\partial w/\partial y|_w$, respectively.
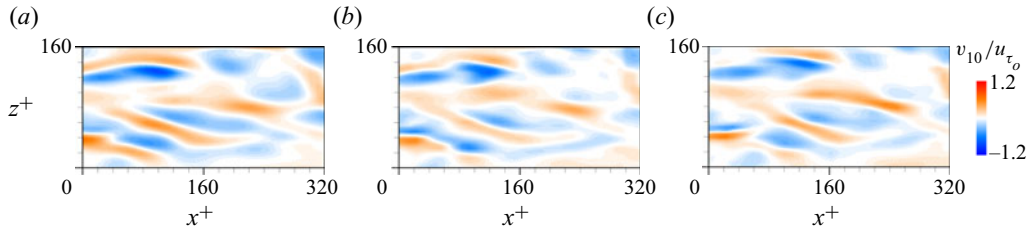
FIGURE 9. Contours of the instantaneous v_{10} from the controlled flow by opposition control: (a) v_{10}^{true}; (b) σv_{10}^{pred} from $\chi_w = p_w$; (c) σv_{10}^{pred} from $\chi_w = \partial w/\partial y|_w$.
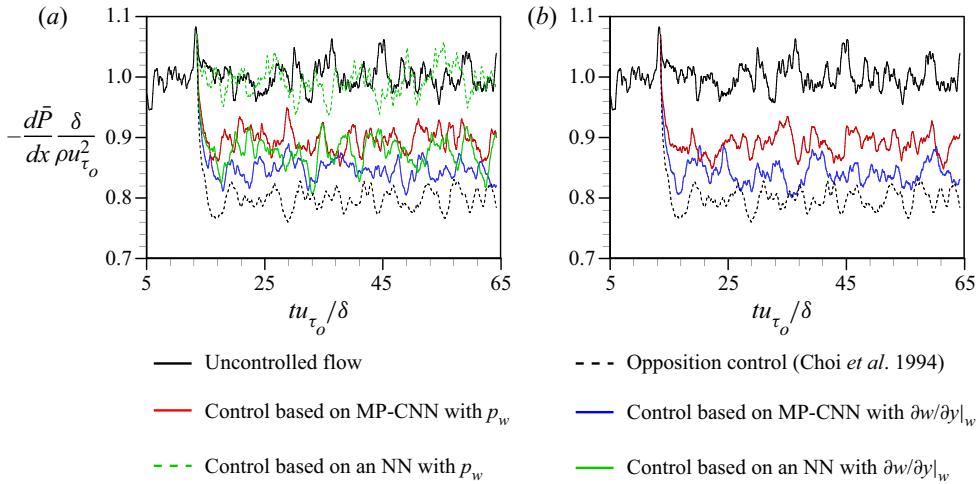

FIGURE 10. Time histories of the mean pressure gradient in a turbulent channel flow at $Re_\tau = 178$: (a) MP-CNN and NN trained with the uncontrolled flow; (b) MP-CNN trained with the controlled flow.

Figure 10 shows the time histories of the mean pressure gradient for the controls based on MP-CNNs with $\chi_w = p_w$ and $\partial w/\partial y|_w$, together with those based on a neural network (NN). Here, we show the results from two different MP-CNNs, one trained with the uncontrolled flow and the other trained with the controlled flow by opposition control, respectively. For the first MP-CNN, we apply $v_w = -\sigma v_{10}^{pred}$, and for the latter, $v_w = -v_{10}^{pred}$. The NN considered has one hidden layer and one neurone (the output of this NN is one point v_{10}), which is the same model as that of Lee *et al.* (1997). With opposition control, the drag is reduced by approximately 20 % from that of the uncontrolled flow. Note that this amount of drag reduction is smaller than 25 % reported by Choi *et al.* (1994). This difference may come from a numerical set-up such as the spatial discretization method and grid resolution. In particular, Chang *et al.* (2002) and Chung & Talha (2011) also reported approximately 20 % drag reduction with $v_w = -v_{10}$ at the same Reynolds number.

When MP-CNN trained with the controlled flow is applied, the drag is reduced by 11 % and 16 % with $\chi_w = p_w$ and $\partial w/\partial y|_w$, respectively (figure 10b). By the NN trained with the controlled flow, v_{10}^{pred} continues to grow with $v_w = -v_{10}^{pred}$, and the simulation eventually diverges unless the magnitude of v_w is forced to be smaller than a predetermined constant. In the case of MP-CNN trained with the uncontrolled flow, the amounts of drag

reduction are 10 % and 15 % with $\chi_w = p_w$ and $\partial w/\partial y|_w$, respectively (figure 10a), which are slightly lower than those by MP-CNN trained with the controlled flow. This result indicates an excellent capability of reducing drag by the present MP-CNN trained with the uncontrolled flow. By the NN trained with the uncontrolled flow, the amounts of drag reduction are approximately 0 % and 12 %, respectively, for $\chi_w = p_w$ and $\partial w/\partial y|_w$, suggesting that the control performance of the NN depends more on the choice of the input variable than that of MP-CNN, and is not better than that of MP-CNN. We also conduct controls using MP-CNN trained with the uncontrolled flow for $\chi_w = \partial u/\partial y|_w$, and obtain 5 % drag reduction. Although v_{10}^{pred} with $\chi_w = \partial u/\partial y|_w$ is not quite similar to v_{10}^{true}, drag reduction still occurs albeit its small amount. On the other hand, the amounts of drag reduction with $\chi_w = p_w$ and $\partial w/\partial y|_w$ are different from each other, even though their MP-CNN's have similar prediction performance for the controlled flow. This is due to the different sensitivity of p_w and $\partial w/\partial y|_w$ to the wall actuation. That is, as shown in figure 8, the slope of a fitting line for $\chi_w = \partial w/\partial y|_w$ is closer to 1 than that for $\chi_w = p_w$. Also, $v_{10,rms}^{pred}/v_{10,rms}^{true}$ from $\chi_w = \partial w/\partial y|_w$ is 1.6, but it is 2.2 from $\chi_w = p_w$.

4.2. *Improving the control performance by filtering small to intermediate scales*

Although the control based on the present MP-CNN performs quite well, the drag-reduction performance is still lower than that of opposition control. In this section we explain the reason for this lower drag reduction by MP-CNN and suggest a way to improve the drag-reduction performance.

Figure 11 shows the streamwise and spanwise energy spectra of v_{10}^{true} and v_{10}^{pred}'s for the controlled flow by MP-CNN trained with the uncontrolled flow. As shown, the energy spectra of v_{10}^{pred}'s for p_w and $\partial w/\partial y|_w$ at low wavenumbers are quite similar to those of v_{10}^{true}, but the energy spectra of v_{10}^{pred} for $\partial u/\partial y|_w$ at all wavenumbers and for p_w and $\partial w/\partial y|_w$ at intermediate to high wavenumbers are quite different from those of v_{10}^{true}. Therefore, the intermediate to high wavenumber components of v_{10}^{pred} may degrade the drag-reduction performance of the MP-CNN control. To test this conjecture, we remove some length scales of v_{10}^{pred} by applying three different low-pass filters, where the cut-off wavenumbers are $(k_{x,c}^+, k_{z,c}^+) \approx (0.150, 0.540)$, $(0.075, 0.270)$ and $(0.038, 0.135)$, respectively (hereafter, v_{10} with a low-pass filter is called $\tilde{v}_{10}$). The opposition control, $v_w = -\tilde{v}_{10}^{true}$, with the smallest cut-off wavenumbers $(k_{x,c}^+, k_{z,c}^+) = (0.038, 0.135)$ provides 18 % drag reduction, as opposed to 20 % drag reduction by the control with all the wavenumber components. Lorang *et al.* (2008) also showed that opposition controls with the POD- or Fourier-truncated v_{10} provided 15 % and 8 % drag reductions, respectively, where the first streamwise and first three spanwise modes of the POD and Fourier coefficients were used. The control by MP-CNN with a low-pass filter is $v_w = -\tilde{\sigma}\,\tilde{v}_{10}^{pred}$, where $\tilde{\sigma} = 0.5 v_{10,rms}^{true}(\text{uncontrolled})/\tilde{v}_{10,rms}^{pred}$. Table 1 shows the variation of the drag-reduction rate with the low-pass filter, together with that of opposition control (Choi *et al.* 1994). The low-pass filter at $(k_{x,c}^+, k_{z,c}^+) = (0.038, 0.135)$ enhances the control performance for all three input wall variables. Especially, the amount of drag reduction by $\partial w/\partial y|_w$ is quite comparable (18 %) to that by opposition control. Although the controls with low-pass filters at higher cut-off wavenumbers are less effective, the amounts of drag reduction are still meaningfully large. These results indicate that the intermediate to high wavenumber components of v_{10}^{pred} degrade the drag-reduction performance, and an elimination of those components enhances the drag-reduction performance.
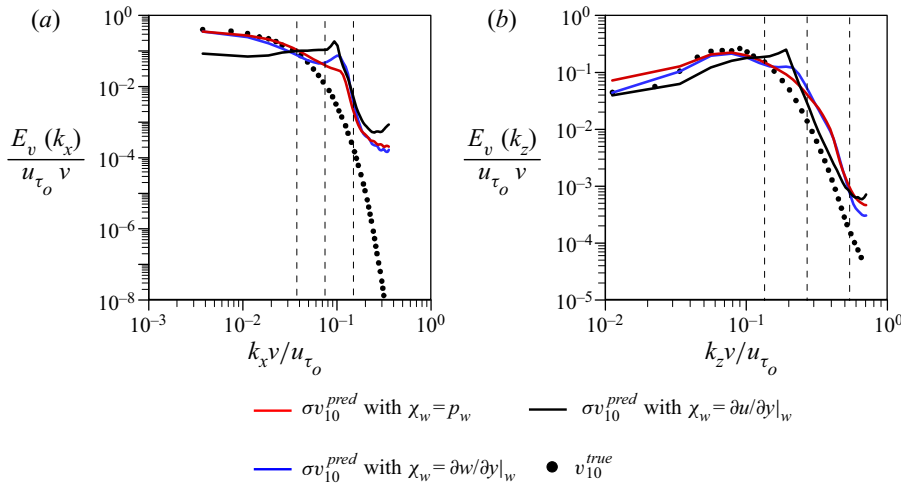
FIGURE 11. Energy spectra of v_{10} from the controlled flow by MP-CNN: (*a*) streamwise wavenumber; (*b*) spanwise wavenumber. Here, v_{10}^{pred} and χ_w's are from the controlled flow by MP-CNN trained with the uncontrolled flow, whereas v_{10}^{true} is from the controlled flow by opposition control (Choi *et al.* 1994). Dashed lines in (*a*) denote $k_x^+ = 0.038, 0.075$ and 0.150, and those in (*b*) correspond to $k_z^+ = 0.135, 0.270$ and 0.540, respectively.

$(k_{x,c}^+, k_{z,c}^+)$	DR (%) with the opposition control	DR (%) with MP-CNN		
		$\chi_w = p_w$	$\chi_w = \dfrac{\partial u}{\partial y}\Big|_w$	$\chi_w = \dfrac{\partial w}{\partial y}\Big|_w$
Without filter	20	10	5	15
(0.150, 0.540)	20	14	6	14
(0.075, 0.270)	20	15	6	13
(0.038, 0.135)	18	17	11	18

TABLE 1. Variation of the drag-reduction rate (DR) by MP-CNN with the low-pass filter applied to v_{10}^{pred}, together with that by opposition control. $k_{x,c}^+$ and $k_{z,c}^+$ are the streamwise and spanwise cut-off wavenumbers, respectively.

4.3. *Control based on all three wall-variable sensing*

In this section we train MP-CNN using all three wall variables (p_w, $\partial u/\partial y|_w$ and $\partial w/\partial y|_w$) with the uncontrolled flow at $Re_\tau = 178$ (called MP-CNN3 hereafter) instead of using one of them as the input. The only difference in this MP-CNN3 from MP-CNN is the input size, i.e. $32 \times 32 \times 3$ instead of 32×32. For the uncontrolled flow, the correlation from MP-CNN3 is $\rho_{v_{10}} = 0.99$, which is higher than those from MP-CNN using single χ_w ($\rho_{v_{10}} = 0.96, 0.92$ and 0.96 for $\chi_w = p_w$, $\partial u/\partial y|_w$ and $\partial w/\partial y|_w$, respectively), indicating that more input wall variables provide a higher correlation with v_{10}^{true} for the uncontrolled flow. On the other hand, for the controlled flow, the scatter plot of v_{10}^{true} and v_{10}^{pred} from MP-CNN3 (figure 12*a*) demonstrates that its correlation ($\rho_{v_{10}} = 0.83$) is very similar to those ($\rho_{v_{10}} = 0.85$ and 0.84) from MP-CNNs with $\chi_w = p_w$ and $\partial w/\partial y|_w$, respectively,
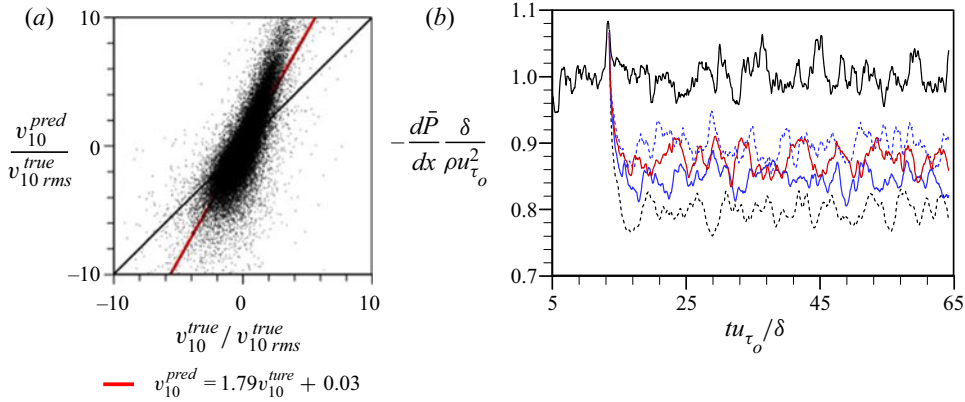
FIGURE 12. Scatter plot of v_{10}^{true} and v_{10}^{pred} from MP-CNN3 (controlled flow) and mean pressure gradient at $Re_\tau = 178$: (*a*) scatter plot; (*b*) mean pressure gradient. In (*a*) a black line denotes the slope of 1, and a red line is a fitting line for the scatter plot and is given at the bottom of the figure. In (*b*), black line, uncontrolled flow; black dashes, opposition control (Choi *et al.* 1994); red line, control by MP-CNN3; blue dashes, control by MP-CNN with p_w; blue line, control by MP-CNN with $\partial w / \partial y|_w$.

but its slope of the fitting line is larger than that from MP-CNN with $\chi_w = \partial w / \partial y|_w$ and slightly smaller than that with $\chi_w = p_w$ (see also figure 8).

We apply MP-CNN3 to the control with $v_w = -\sigma v_{10}^{pred}$ (4.1). The amount of drag reduction by this MP-CNN3 is 12 %, which is higher and lower than those obtained by MP-CNNs trained with $\chi_w = p_w$ and $\partial w / \partial y|_w$, respectively (figure 12*b*). This result indicates that a good prediction of the correlation by a CNN for uncontrolled flow does not guarantee a good performance in the present feedback control. A similar inconsistency has been also observed with *a priori* and *a posteriori* tests of a subgrid-scale model in large eddy simulation (Park, Yoo & Choi 2005).

5. Application to a higher Reynolds number flow

In this section we investigate if MP-CNN trained at a low Reynolds number can maintain the prediction capability and drag-reduction performance for a higher Reynolds number flow. A higher Reynolds number considered is $Re_\tau = 578$, but MP-CNN is trained at $Re_\tau = 178$. We conduct a direct numerical simulation for a turbulent channel flow at $Re_\tau = 578$. The computational domain size is $\pi\delta(x) \times 2\delta(y) \times 0.5\pi\delta(z)$, and the grid resolutions are $\Delta x^+ \approx 9.5$ and $\Delta z^+ \approx 4.7$, respectively. These grid resolutions in wall units are very similar to but not the same as those at $Re_\tau = 178$ ($\Delta x^+ \approx 8.7$ and $\Delta z^+ \approx 4.4$). As we show below, this small difference in wall units does not affect the prediction of v_{10} at $Re_\tau = 578$. However, the numbers of grid points for the input (χ_w) and output (v_{10}^{pred}) of MP-CNN should be taken to be the same as those at $Re_\tau = 178$, i.e. 32×32 and 16×16, respectively. The input and output of MP-CNN are normalized as in (2.4*a,b*): $\chi_w^* = (\chi_w - \langle \chi_w \rangle) / \chi_{w,rms}$ and $v_{10}^{pred*} = v_{10}^{pred} / v_{10,rms}^{true}$. Another MP-CNN is separately trained with the flow at $Re_\tau = 578$ to estimate the prediction capability of MP-CNN trained at $Re_\tau = 178$. Hereafter, MP-CNN178 and MP-CNN578 represent MP-CNNs trained at $Re_\tau = 178$ and 578, respectively.
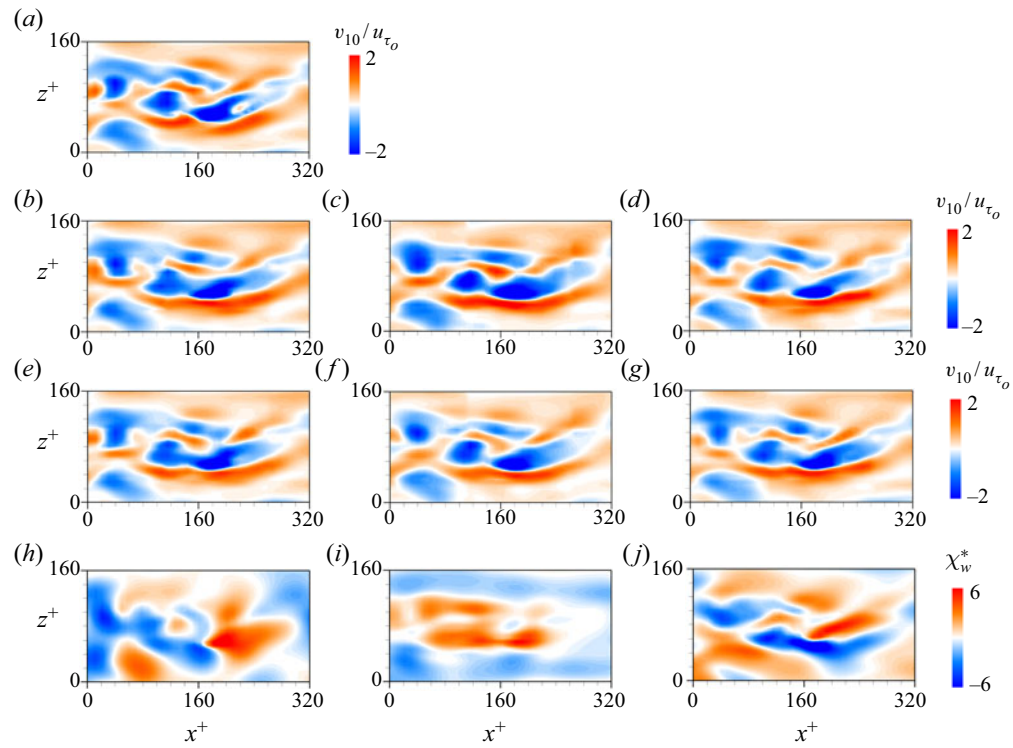
FIGURE 13. Contours of the instantaneous v_{10} and χ_w's at $Re_\tau = 578$ (uncontrolled flow): (a) v_{10}^{true}; (b–d) v_{10}^{pred} by MP-CNN178; (e–g) v_{10}^{pred} by MP-CNN578; (h) p_w; (i) $\partial u/\partial y|_w$; (j) $\partial w/\partial y|_w$. The input wall variables for (b,e), (c,f) and (d,g) are $\chi_w = p_w$, $\partial u/\partial y|_w$ and $\partial w/\partial y|_w$, respectively.

	Opposition control	MP-CNN178			MP-CNN578		
χ_w		p_w	$\dfrac{\partial u}{\partial y}\bigg|_w$	$\dfrac{\partial w}{\partial y}\bigg|_w$	p_w	$\dfrac{\partial u}{\partial y}\bigg|_w$	$\dfrac{\partial w}{\partial y}\bigg|_w$
DR (%)	19	10	4	15	11	6	14

TABLE 2. Drag-reduction rates with MP-CNN178 and MP-CNN578 at $Re_\tau = 578$.

Figure 13 shows the instantaneous v_{10}'s at $Re_\tau = 578$ from DNS and predicted by MP-CNN178 and MP-CNN578 with $\chi_w = p_w$, $\partial u/\partial y|_w$ and $\partial w/\partial y|_w$, respectively. The correlation coefficients between v_{10}^{true} and v_{10}^{pred}'s by MP-CNN178 with p_w, $\partial u/\partial y|_w$ and $\partial w/\partial y|_w$ are 0.94, 0.90 and 0.94, respectively, whereas those by MP-CNN578 are 0.95, 0.91 and 0.95, respectively. Hence, MP-CNN178 predicts not only the magnitude of v_{10} but also its spatial distribution at $Re_\tau = 578$. This is because the flow near the wall is well scaled in wall units (Hoyas & Jiménez 2006; Jiménez 2013).

Finally, we apply MP-CNN178 to the control of a turbulent channel flow at $Re_\tau = 578$. The control method is the same as in § 4.1. Table 2 shows the drag-reduction rates from MP-CNN178 and MP-CNN578. We obtain 10 %, 4 % and 15 % drag reductions by the

controls based on MP-CNN178 with $\chi_w = p_w$, $\partial u/\partial y|_w$ and $\partial w/\partial y|_w$, respectively. These amounts of drag reduction are nearly the same as those from the controls based on MP-CNN578. Therefore, the present MP-CNN is found to maintain the prediction and control capabilities even for a higher Reynolds number flow.

6. Conclusions

In the present study we applied convolutional neural networks to predict the wall-normal velocity at $y^+ = 10$ (v_{10}) from the spatial information of the wall variables such as $\chi_w = p_w$, $\partial u/\partial y|_w$ and $\partial w/\partial y|_w$. A CNN was trained with uncontrolled turbulent channel flow at $Re_\tau = 178$ for each of the three wall variables. The correlation coefficients between true and predicted v_{10}'s (v_{10}^{true} and v_{10}^{pred}, respectively) were 0.95, 0.90 and 0.95 for $\chi_w = p_w$, $\partial u/\partial y|_w$ and $\partial w/\partial y|_w$, respectively, when the convolutional neural networks were trained to predict v_{10} at a point from a spatial distribution of χ_w. When we further improved convolutional neural networks to predict a spatial distribution of v_{10} for the elimination of local oscillations that existed in v_{10}^{pred}, the correlation coefficients slightly increased to be 0.96, 0.92 and 0.96, respectively, and the small scales of v_{10} were better predicted. The improved convolutional neural networks were applied to the control of turbulent channel flow for skin-friction drag reduction, $v_w = -\sigma v_{10}^{pred}$, where $\sigma = 0.5\, v_{10,rms}^{true}$ (uncontrolled)$/v_{10,rms}^{pred}$. Drag reductions were 10 %, 5 %, 15 % by the convolutional neural networks with $\chi_w = p_w$, $\partial u/\partial y|_w$ and $\partial w/\partial y|_w$, respectively. Note that the present approach is different from those of the previous studies (Lee *et al.* 1997; Lorang *et al.* 2008), in that the present approach trained convolutional neural networks using the uncontrolled flow, while the previous ones used controlled flows for training neural networks. The lower drag reductions obtained by the present CNN were caused by its over-prediction of small to intermediate scales of v_{10}. An elimination of these scales by applying a low-pass filter increased the drag-reduction rates up to 18 % whose amount is comparable to that of opposition control (Choi *et al.* 1994). We also applied a CNN based on all three wall variables (p_w, $\partial u/\partial y|_w$ and $\partial w/\partial y|_w$), but the control performance based on this CNN was lower than that with $\chi_w = \partial w/\partial y|_w$ alone. Finally, convolutional neural networks trained at $Re_\tau = 178$ were applied to control a higher Reynolds number flow ($Re_\tau = 578$), resulting in similar amounts of drag reduction, showing the prediction and control capability of the present convolutional neural networks.

In the present numerical study the size of the input wall variable is $l_x^+ \approx 270$ and $l_z^+ \approx 135$ with the resolution of $\Delta l_x^+ \approx 8.7$ and $\Delta l_z^+ \approx 4.4$. In experiments, Yamagami, Suzuki & Kasagi (2005) measured $\partial u/\partial y|_w$ along the spanwise direction ($l_z^+ \approx 170$ with $\Delta l_z^+ \approx 10$), Yoshino, Suzuki & Kasagi (2008) conducted a feedback control by measuring $\partial u/\partial y|_w$ along the spanwise direction ($l_z^+ \approx 560$ with $\Delta l_z^+ \approx 12$), and Mäteling, Klaas & Schröder (2020) measured both $\partial u/\partial y|_w$ and $\partial w/\partial y|_w$ in the streamwise and spanwise directions ($l_x^+ \approx 90$ and $l_z^+ \approx 50$ with $\Delta l_x^+ \approx 6$ and $\Delta l_z^+ \approx 6$). Therefore, the present feedback control may be realized experimentally.

In the present study we applied convolutional neural networks to the control of turbulent channel flow in the framework of opposition control, and, thus, the drag-reduction performance cannot surpass that of original opposition control (Choi *et al.* 1994). Thus, the next step may be to develop a machine learning method, not relying on opposition control. One of the promising methods is to train a CNN with a reinforcement learning algorithm (Silver *et al.* 2016) which finds the best control input (blowing and suction at the wall) for a given state (wall variables) to get maximum reward (drag reduction). In this

case, the CNN should be trained during control, and the loss function can be, for example, skin-friction drag itself or Reynolds shear stress near the wall. The control performance of this approach may be compared with those of the optimal and suboptimal controls (Abergel & Temam 1990; Choi *et al.* 1993; Lee *et al.* 1998; Bewley, Moin & Temam 2001; Lee *et al.* 2001).

Acknowledgements

Declaration of interests

The authors report no conflict of interest.

Appendix A. Other machine learning techniques and their prediction performance

We compare the performance of the CNN with that of other machine learning techniques such as the least absolute shrinkage and selection operator (Lasso), random forest (RF), and FCNN. The outputs from these techniques are v_{10}^{pred} at a point as described in § 2.1. The Lasso (Tibshirani 1996) is a linear model, which approximates v_{10} as $v_{10}^{pred} = w_0 + \sum_{j=1}^{n} w_j \chi_{wj}$, where w_j's ($j = 0, 1, 2, \ldots, n$) are the weight parameters to be optimized. The loss function is the sum of the quadratic error and L1 norm regularization term ($= \lambda \sum_{j=0}^{n} |w_j|$) with $\lambda = 0.01$ in this study. The RF (Breiman 2001) is ensemble-averaged decision trees, and these trees are composed of if-then-else binary decision nodes. The depth and number of trees (d_{RF} and N_{RF}, respectively) are major user-defined parameters, and we select $d_{RF} = 30$ and $N_{RF} = 30$. The FCNN is the most basic architecture of the neural network, and we use four hidden layers with 256 neurones per layer. Table 3 shows that the numbers of hidden layers and neurones used are sufficient for the present prediction problem. The loss function and method for optimization are the same as those of the CNN. The user-defined parameters in Lasso and RF are also selected from several parametric studies.

Figure 14 shows the variations of the quadratic error (the first term on the right-hand side of (2.5)) and correlation coefficient between v_{10}^{true} and v_{10}^{pred} with the machine learning techniques and input wall variables. The prediction performance of the Lasso is the worst among the machine learning techniques investigated, because it is a linear representation. The RF has better performance than Lasso, but does not significantly improve the performance. On the other hand, the predictions are greatly improved by the neural networks, especially by the CNN. The prediction of the CNN is better than that of the FCNN, because convolution operations are more appropriate to recognize local patterns of an image-like input than fully connected structures (LeCun *et al.* 2015).

Appendix B. Parametric study on 1P-CNN

Figure 15 shows the schematic diagram of 1P-CNN for v_{10}^{pred} at a point, as described in § 2.3. There are many parameters to determine the prediction performance of 1P-CNN, e.g. the number of the residual blocks, the dimensions of the feature maps and the number of training data. When the number of training data is sufficient, the CNN with the residual blocks continues to improve the prediction performance as the number of hidden layers

(N_{hl}, N_{nr})	$\chi_w = p_w$	$\chi_w = \left.\dfrac{\partial u}{\partial y}\right\|_w$	$\chi_w = \left.\dfrac{\partial w}{\partial y}\right\|_w$
(1, 1024)	0.80	0.76	0.90
(2, 512)	0.85	0.80	0.92
(3, 256)	0.86	0.80	0.92
(3, 512)	0.87	0.80	0.93
(4, 128)	0.86	0.80	0.92
(4, 256)	0.87	0.80	0.93
(4, 512)	0.87	0.80	0.93
(8, 512)	0.87	0.80	0.92

TABLE 3. Variation of the correlation coefficients ($\rho_{v_{10}}$) between v_{10}^{true} and v_{10}^{pred} (FCNNs) with the numbers of hidden layers (N_{hl}) and neurones per layer (N_{nr}).
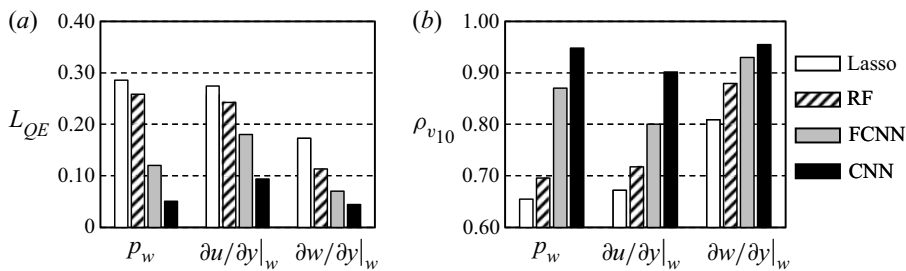

FIGURE 14. Prediction performance of machine learning techniques with the input wall variables: (*a*) quadratic error; (*b*) correlation coefficient between v_{10}^{true} and v_{10}^{pred}.
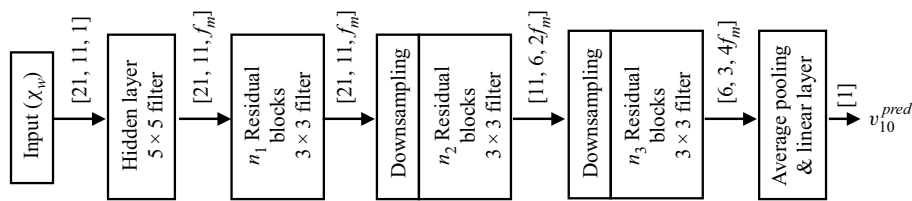

FIGURE 15. Schematic diagram of 1P-CNN with residual blocks. After one hidden layer behind the input wall variable, we locate n_1, n_2 and n_3 residual blocks, and change the dimensions of the feature maps. For example, from n_1 to n_2 residual blocks, [21, 11, f_m] are changed to [11, 6, $2f_m$]. Note that one residual block consists of two hidden layers, as described in the caption of figure 3.

increases, unlike the CNN without the residual block (He *et al.* 2015). Therefore, we first set the maximum number of training data to be approximately three times ($N_{train} = 3.8 \times 10^6$) that used in the ImageNet large-scale visual recognition challenge.

Table 4 and figure 16 show the variations of the correlation coefficient between v_{10}^{true} and v_{10}^{pred} and the quadratic error with the parameters of 1P-CNN, respectively. First, we change the number of the residual blocks from $(n_1, n_2, n_3) = (1, 1, 1)$ to $(4, 4, 4)$. As shown,

Case	N_{train}	n_1	n_2	n_3	N_{hl}	f_m	$\rho_{v_{10}}(p_w)$	$\rho_{v_{10}}\left(\left.\dfrac{\partial u}{\partial y}\right\|_w\right)$	$\rho_{v_{10}}\left(\left.\dfrac{\partial w}{\partial y}\right\|_w\right)$
CNN_{ref}	3.8×10^6	3	2	3	17	16	0.95	0.90	0.95
CNN_{111}	3.8×10^6	1	1	1	7	16	0.92	0.87	0.94
CNN_{222}	3.8×10^6	2	2	2	13	16	0.94	0.89	0.95
CNN_{444}	3.8×10^6	4	4	4	25	16	0.95	0.91	0.96
CNN_{f8}	3.8×10^6	3	2	3	17	8	0.93	0.88	0.95
CNN_{f24}	3.8×10^6	3	2	3	17	24	0.95	0.91	0.96
$CNN_{0.5M}$	0.5×10^6	3	2	3	17	16	0.93	0.86	0.94
CNN_{1M}	1×10^6	3	2	3	17	16	0.94	0.88	0.95
CNN_{2M}	2×10^6	3	2	3	17	16	0.94	0.89	0.95
CNN_{5M}	5×10^6	3	2	3	17	16	0.95	0.90	0.96

TABLE 4. Variations of the correlation coefficient between v_{10}^{true} and v_{10}^{pred} with the parameters of 1P-CNN. Here, n_1, n_2 and n_3 are the numbers of the residual blocks, f_m is the depth of the feature map after the first hidden layer (see figure 15), N_{hl} is the number of total hidden layers and N_{train} is the number of training data ($N_{train} = 1$ contains 21×11 data of χ_w's and one data of v_{10}^{true}). We denote by CNN_{ref} the reference case for comparison.
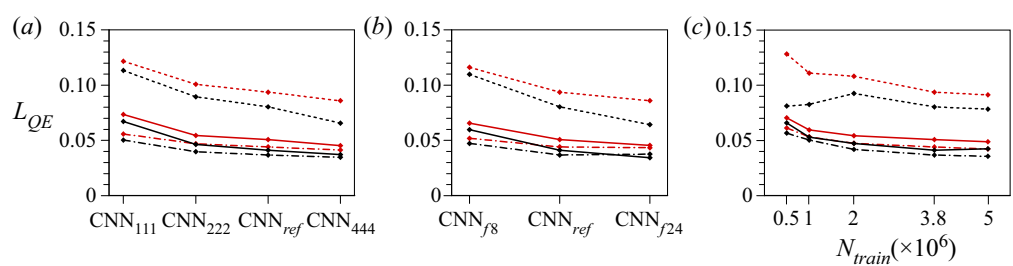

FIGURE 16. Variations of the quadratic error L_{QE} with the parameters used in 1P-CNN: (a) n_1, n_2 and n_3; (b) f_m; (c) N_{train}. ——, p_w; - - - -, $\partial u/\partial y|_w$; $-\cdot-\cdot-$, $\partial w/\partial y|_w$. Black and red lines denote L_{QE}'s for the training and test datasets, respectively.

the correlation and quadratic error nearly converge at $(n_1, n_2, n_3) = (3, 2, 3)$ (reference case), although the quadratic error for $\partial u/\partial y|_w$ requires slightly more residual blocks for convergence. Then, we change the depth of the feature map from $f_m = 8$ to 24, showing that $f_m = 16$ provides reasonable convergence of $\rho_{v_{10}}$ and L_{QE}. Lastly, the number of training data is changed from 0.5×10^6 to 5×10^6. For $\chi_w = \partial u/\partial y|_w$, the quadratic error for the training data shows a non-monotonic behaviour with increasing N_{train}, which is due to the overfitting for $N_{train} \leq 1.0 \times 10^6$. For all of the wall variables, however, the quadratic errors nearly converge at $N_{train} = 3.8 \times 10^6$, indicating that the number of training data used in the present study is adequate for training the CNN_{ref}. Therefore, we conclude that the parameters used for the CNN_{ref} are good enough to predict v_{10} ($\rho_{v_{10}} \geq 0.9$ for all three wall variables considered).
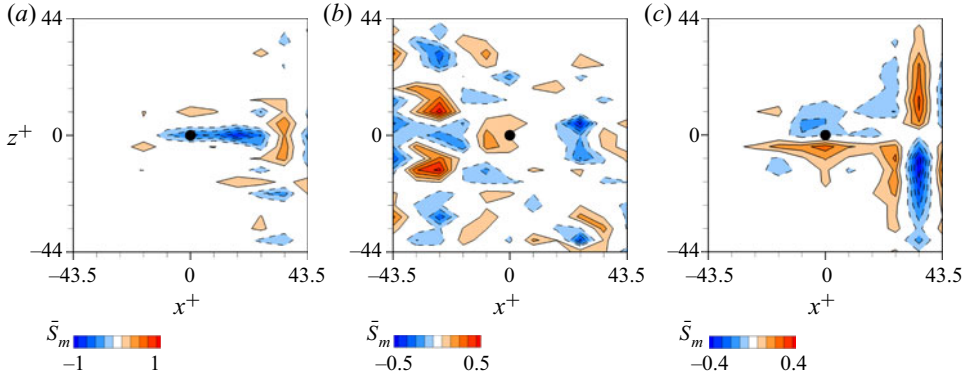
FIGURE 17. Averaged saliency map $\bar{S}_m$ from the CNN4: (a) $\chi_w = p_w$; (b) $\chi_w = \partial u/\partial y|_w$; (c) $\chi_w = \partial w/\partial y|_w$. Solid circles at the origin are the location of v_{10}.

Appendix C. Saliency map for visualizing v_{10}^{pred} with χ_w

The saliency map S_m, proposed by Simonyan *et al.* (2013), of v_{10}^{pred} at a grid point with respect to χ_w at 21×11 grid points is defined as $S_m = \partial v_{10}^{pred*}(\chi_w^*)/\partial \chi_w^*$, where $v_{10}^{pred*} = v_{10}^{pred}/v_{10,rms}^{true}$, and χ_w^* is defined in (2.4a). In the case of a linear model, $v_{10}^{pred*} = w_0 + \sum w_j \chi_{wj}^*$ and, thus, S_m is the same as the weight w_j distribution. Therefore, the saliency maps shown here indicate the dominant patterns of the wall variables correlated with v_{10}^{pred}. We use an averaged saliency map $\bar{S}_m$ over 3.8 million training dataset due to unrecognizable patterns in the instantaneous S_m caused by the nonlinear characteristics of the CNN, where the degree of the nonlinearity depends on the number of hidden layers (see also Kim & Lee 2020). The $\bar{S}_m$ obtained from the present CNN with 17 hidden layers does not provide any meaningful distribution of χ_w due to a highly nonlinear nature of the CNN (see below). Therefore, we additionally train two different convolutional neural networks with lower numbers of hidden layers (4 and 7 hidden layers) for the visualization of the correlation. These convolutional neural networks are called CNN4 and CNN7, respectively, whereas the CNN with 17 hidden layers is called CNN17. The correlation coefficients between v_{10}^{true} and v_{10}^{pred}'s from $\chi_w = p_w$, $\partial u/\partial y|_w$ and $\partial w/\partial y|_w$ are $\rho_{v_{10}} = 0.88$, 0.82 and 0.93 from the CNN4, and 0.90, 0.84 and 0.93 from the CNN7, respectively. These correlations are lower than those from the CNN17.

Figure 17 shows $\bar{S}_m$ from the CNN4 for three input wall variables. For $\chi_w = p_w$, the dominant feature of $\bar{S}_m$ is a narrow region of negative $\bar{S}_m$ elongated in the streamwise direction ($-13 \leq x^+ \leq 30$ near $z^+ = 0$), and also a region of positive $\bar{S}_m$ at $x^+ = 35$. This distribution of $\bar{S}_m$ is quite different from that of the two-point correlation shown in figure 2(a), although the locations of maximum correlation are similar to each other (highest $\bar{S}_m$ and ρ occur at $x^+ = 17$ and 26, respectively). The distribution of $\bar{S}_m$ for $\chi_w = \partial u/\partial y|_w$ is quite noisy and is very different from that of the two-point correlation (figure 2b). It is difficult to extract a meaningful distribution of the correlation from this figure. The distribution of $\bar{S}_m$ for $\chi_w = \partial w/\partial y|_w$ is also very different from that of the two-point correlation (figure 2c), in that maximum $\bar{S}_m$ occurs at $x^+ = 35$ (but local maxima at $z^+ = \pm 4.4$ around $x = 0$ are also captured). Figure 18 shows the spatial distributions of $\bar{S}_m$ from the CNN7 and CNN17 for $\chi_w = p_w$ and $\partial w/\partial y|_w$. The saliency map $\bar{S}_m$ for $\chi_w = \partial u/\partial y|_w$ is not shown here because the patterns are completely unrecognizable. With increasing the number of the hidden layers, the distribution of $\bar{S}_m$
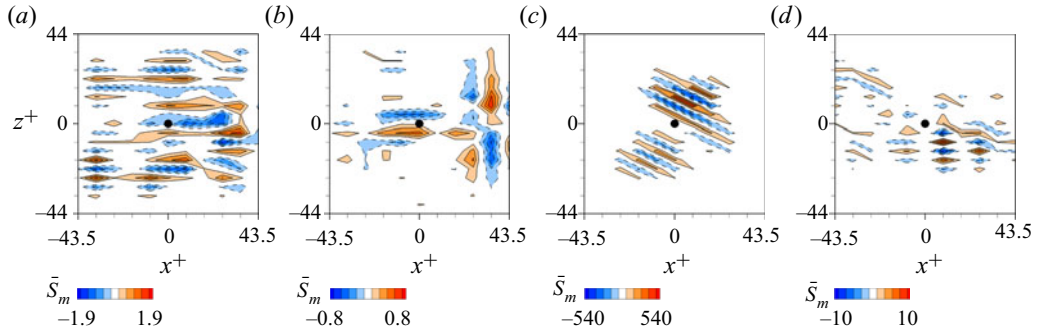
FIGURE 18. Averaged saliency maps $\bar{S}_m$ from the CNN7 and CNN17: (*a*) CNN7 with $\chi_w = p_w$; (*b*) CNN7 with $\chi_w = \partial w / \partial y|_w$; (*c*) CNN17 with $\chi_w = p_w$; (*d*) CNN17 with $\chi_w = \partial w / \partial y|_w$.
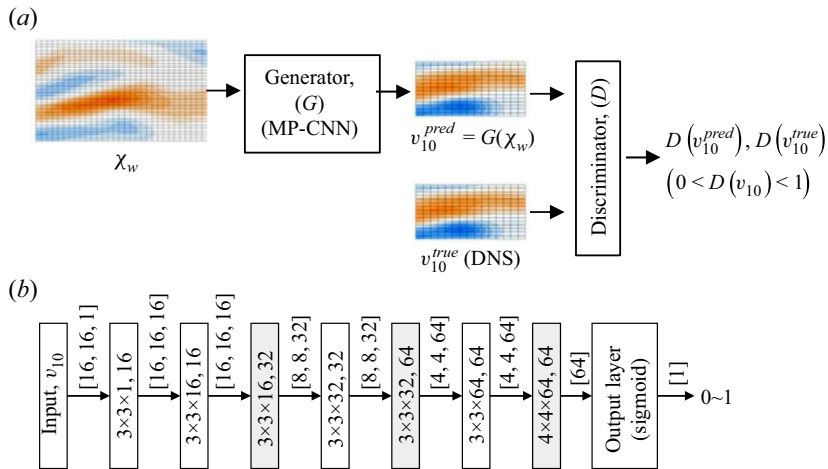

FIGURE 19. Generative adversarial networks used in the present study: (*a*) structure; (*b*) discriminator. In (*b*) the size and number of the filters are given inside each box, and the dimensions of the feature maps are given next to the arrows. Grey boxes in (*b*) are the downsampling layers.

becomes more difficult to interpret, especially for the CNN17. These results indicate that the saliency maps themselves do not necessarily provide important physical relations due to the nonlinearity in the CNN, although they may capture some of physical relations for a certain problem. Therefore, despite the advantage of achieving higher correlations between v_{10}^{true} and v_{10}^{pred} from more hidden layers, it is more difficult to visualize and understand the process within the CNN.

Appendix D. Generative adversarial networks

Figure 19(*a*) shows the structure of the generative adversarial networks (GAN; Goodfellow *et al.* 2014) used in the present study. The generator (G) is MP-CNN, and an additional convolutional neural network (figure 19*b*) is used for the discriminator (D). The discriminator takes v_{10}^{true} or v_{10}^{pred} as the input, and prints out a value between 0 and 1 by using sigmoid function ($f(x) = 1/(1 + e^{-x})$) at the output. The discriminator is used only

for training MP-CNN and is discarded after training. The GAN uses two loss functions:

$$L_{GAN,G} = -\log\left\{D\left(v_{10}^{pred}\right)\right\} \quad \text{for } (G), \tag{D 1}$$

$$L_{GAN,D} = -\log\left\{D\left(v_{10}^{true}\right)\right\} - \log\left\{1 - D\left(v_{10}^{pred}\right)\right\} \quad \text{for } (D). \tag{D 2}$$

In the present study the total loss functions for (G) and (D) are given as $L_{total}(G) = L_{QE} + 0.01L_{GAN,G}$ and $L_{total}(D) = L_{GAN,D}$, respectively, where

$$L_{QE} = \frac{1}{2NN_xN_z} \sum_{l=1}^{N} \sum_{i=1}^{N_x} \sum_{k=1}^{N_z} \left(\frac{v_{10_{i,k,l}}^{true} - v_{10_{i,k,l}}^{pred}}{v_{10,rms}^{true}}\right)^2, \tag{D 3}$$

N is the number of dataset, and N_x and N_z are the numbers of grid points for the output v_{10}^{pred}.

REFERENCES

ABERGEL, F. & TEMAM, R. 1990 On some control problems in fluid mechanics. *Theor. Comput. Fluid Dyn.* **1**, 303–325.

BENGIO, Y. 2012 Practical recommendations for gradient-based training of deep architectures. arXiv:1206.5533.

BEWLEY, T. R., MOIN, P. & TEMAM, R. 2001 DNS-based predictive control of turbulence: an optimal benchmark for feedback algorithms. *J. Fluid Mech.* **447**, 179–225.

BEWLEY, T. R. & PROTAS, B. 2004 Skin friction and pressure: the "footprints" of turbulence. *Physica* D **196**, 28–44.

BREIMAN, L. 2001 Random forests. *Mach. Learn.* **45**, 5–32.

CHANG, Y., COLLIS, S. S. & RAMAKRISHNAN, S. 2002 Viscous effects in control of near-wall turbulence. *Phys. Fluids* **14**, 4069–4080.

CHEVALIER, M., HŒPFFNER, J., BEWLEY, T. R. & HENNINGSON, D. S. 2006 State estimation in wall-bounded flow systems. Part 2. Turbulent flows. *J. Fluid Mech.* **552**, 167–187.

CHOI, H., MOIN, P. & KIM, J. 1994 Active turbulence control for drag reduction in wall-bounded flows. *J. Fluid Mech.* **262**, 75–110.

CHOI, H., TEMAM, R., MOIN, P. & KIM, J. 1993 Feedback control for unsteady flow and its application to the stochastic Burgers equation. *J. Fluid Mech.* **253**, 509–543.

CHUNG, Y. M. & TALHA, T. 2011 Effectiveness of active flow control for turbulent skin friction drag reduction. *Phys. Fluids* **23**, 025102.

GLOROT, X. & BENGIO, Y. 2010 Understanding the difficulty of training deep feedforward neural networks. In *Proceedings of the Thirteenth International Conference on Artificial Intelligence and Statistics* (ed. Y. Teh & M. Titterington), Proceedings of Machine Learning Research, vol. 9, pp. 249–256. PMLR.

GOODFELLOW, I. J., POUGET-ABADIE, J., MIRZA, M., XU, B., WARDE-FARLEY, D., OZAIR, S., COURVILLE, A. & BENGIO, Y. 2014 Generative adversarial networks. arXiv:1406.2661.

GÜEMES, A., DISCETTI, S. & IANIRO, A. 2019 Sensing the turbulent large-scale motions with their wall signature. *Phys. Fluids* **31**, 125112.

HAMMOND, E. P., BEWLEY, T. R. & MOIN, P. 1998 Observed mechanisms for turbulence attenuation and enhancement in opposition-controlled wall-bounded flows. *Phys. Fluids* **10**, 2421–2423.

HE, K., ZHANG, X., REN, S. & SUN, J. 2015 Deep residual learning for image recognition. arXiv:1512.03385.

HŒPFFNER, J., CHEVALIER, M., BEWLEY, T. R. & HENNINGSON, D. S. 2005 State estimation in wall-bounded flow systems. Part 1. Perturbed laminar flows. *J. Fluid Mech.* **534**, 263–294.

HOYAS, S. & JIMÉNEZ, J. 2006 Scaling of the velocity fluctuations in turbulent channels up to $Re_\tau = 2003$. *Phys. Fluids* **18**, 011702.

ILLINGWORTH, S. J., MONTY, J. P. & MARUSIC, I. 2018 Estimating large-scale structures in wall turbulence using linear models. *J. Fluid Mech.* **842**, 146–162.

IOFFE, S. & SZEGEDY, C. 2015 Batch normalization: accelerating deep network training by reducing internal covariate shift. arXiv:1502.03167.

IWAMOTO, K., SUZUKI, Y. & KASAGI, N. 2002 Reynolds number effect on wall turbulence: toward effective feedback control. *Intl J. Heat Fluid Flow* **23**, 678–689.

JIMÉNEZ, J. 2013 Near-wall turbulence. *Phys. Fluids* **25**, 101302.

KASAGI, N., SUZUKI, Y. & FUKAGATA, K. 2008 Microelectromechanical systems-based feedback control of turbulence for skin friction reduction. *Annu. Rev. Fluid Mech.* **41**, 231–251.

KIM, E. & CHOI, H. 2017 Linear proportional-integral control for skin-friction reduction in a turbulent channel flow. *J. Fluid Mech.* **814**, 430–451.

KIM, J. & LEE, C. 2020 Prediction of turbulent heat transfer using convolutional neural networks. *J. Fluid Mech.* **882**, A18.

KINGMA, D. P. & BA, J. 2014 Adam: a method for stochastic optimization. arXiv:1412.6980.

KRIZHEVSKY, A., SUTSKEVER, I. & HINTON, G. E. 2012 ImageNet classification with deep convolutional neural networks. In *Proceedings of the 25th International Conference on Neural Information Processing Systems* (ed. F. Pereira, C. J. C. Burges & L. Bottou), pp. 1097–1105. Curran Associates Inc.

LECUN, Y., BENGIO, Y. & HINTON, G. E. 2015 Deep learning. *Nature* **521**, 436–444.

LECUN, Y., BOSER, B., DENKER, J. S., HENDERSON, D., HOWARD, R. E., HUBBARD, W. & JACKEL, L. D. 1989 Handwritten digit recognition with a back-propagation network. In *Proceedings of the 2nd International Conference on Neural Information Processing Systems* (ed. D. S. Touretzky), pp. 396–404. MIT Press.

LEDIG, C., THEIS, L., HUSZÁR, F., CABALLERO, J., CUNNINGHAM, A., ACOSTA, A., AITKEN, A., TEJANI, A., TOTZ, J., WANG, Z., *et al.* 2016 Photo-realistic single image super-resolution using a generative adversarial network. arXiv:1609.04802.

LEE, K. H., CORTELEZZI, L., KIM, J. & SPEYER, J. 2001 Application of reduced-order controller to turbulent flows for drag reduction. *Phys. Fluids* **13**, 1321–1330.

LEE, C., KIM, J., BABCOCK, D. & GOODMAN, R. 1997 Application of neural networks to turbulence control for drag reduction. *Phys. Fluids* **9**, 1740–1747.

LEE, C., KIM, J. & CHOI, H. 1998 Suboptimal control of turbulent channel flow for drag reduction. *J. Fluid Mech.* **358**, 245–258.

LEE, S. & YOU, D. 2019 Data-driven prediction of unsteady flow over a circular cylinder using deep learning. *J. Fluid Mech.* **879**, 217–254.

LORANG, L. V., PODVIN, B. & LE QUÉRÉ, P. 2008 Application of compact neural network for drag reduction in a turbulent channel flow at low Reynolds numbers. *Phys. Fluids* **20**, 045104.

MÄTELING, E., KLAAS, M. & SCHRÖDER, W. 2020 Simultaneous stereo PIV and MPS^3 wall-shear stress measurements in turbulent channel flow. *Optics* **1**, 40–51.

MILANO, M. & KOUMOUTSAKOS, P. 2002 Neural network modeling for near wall turbulent flow. *J. Comput. Phys.* **182**, 1–26.

NAIR, V. & HINTON, G. E. 2010 Rectified linear units improve restricted Boltzmann machines. In *Proceedings of the 27th International Conference on Machine Learning* (ed. J. Fürnkranz & T. Joachims), pp. 807–814. Omnipress.

OEHLER, S. F., GARCIA-GUTIÉRREZ, A. & ILLINGWORTH, S. J. 2018 Linear estimation of coherent structures in wall-bounded turbulence at $Re_\tau = 2000$. *J. Phys.: Conf. Ser.* **1001**, 012006.

OEHLER, S. F. & ILLINGWORTH, S. J. 2018 Linear estimation and control of coherent structures in wall-bounded turbulence at $Re_\tau = 2000$. In *Proceedings of the 21st Australasian Fluid Mechanics Conference* (ed. T. C. W. Lau & R. M. Kelso). AFMS.

PARK, N., YOO, J. & CHOI, H. 2005 Toward improved consistency of *a priori* tests with *a posteriori* tests in large eddy simulation. *Phys. Fluids* **17**, 015103.

PODVIN, B. & LUMLEY, J. 1998 Reconstructing the flow in the wall region from wall sensors. *Phys. Fluids* **10**, 1182–1190.

REBBECK, H. & CHOI, K.-S. 2001 Opposition control of near-wall turbulence with a piston-type actuator. *Phys. Fluids* **13**, 2142–2145.

REBBECK, H. & CHOI, K.-S. 2006 A wind-tunnel experiment on real-time opposition control of turbulence. *Phys. Fluids* **18**, 035103.

RUMELHART, D. E., HINTON, G. E. & WILLIAMS, R. J. 1986 Learning representations by back-propagating errors. *Nature* **323**, 533–536.

RUSSAKOVSKY, O., DENG, J., SU, H., KRAUSE, J., SATHEESH, S., MA, S., HUANG, Z., KARPATHY, A., KHOSLA, A., BERNSTEIN, M., *et al.* 2015 ImageNet large scale visual recognition challenge. *Intl J. Comput. Vis.* **115**, 211–252.

SILVER, D., HUANG, A., MADDISON, C. J., GUEZ, A., SIFRE, L., VAN DEN DRIESSCHE, G., SCHRITTWIESER, J., ANTONOGLOU, I., PANNEERSHELVAM, V., LANCTOT, M., *et al.* 2016 Mastering the game of Go with deep neural networks and tree search. *Nature* **529**, 484–489.

SIMONYAN, K., VEDALDI, A. & ZISSERMAN, A. 2013 Deep inside convolutional networks: visualising image classification models and saliency maps. arXiv:1312.6034.

SIMONYAN, K. & ZISSERMAN, A. 2014 Very deep convolutional networks for large-scale image recognition. arXiv:1409.1556.

SINGH, P. & MANURE, A. 2019 *Learn Tensorflow 2.0: Implement Machine Learning and Deep Learning Models with Python*. Apress.

SZEGEDY, C., LIU, W., JIA, Y., SERMANET, P., REED, S., ANGUELOV, D., ERHAN, D., VANHOUCKE, V. & RABINOVICH, A. 2014 Going deeper with convolutions. arXiv:1409.4842.

TIBSHIRANI, R. 1996 Regression shrinkage and selection via the Lasso. *J. R. Stat. Soc. Ser.* B **58**, 267–288.

WANG, Y.-S., HUANG, W.-X. & XU, C.-X. 2016 Active control for drag reduction in turbulent channel flow: the opposition control schemes revisited. *Fluid Dyn. Res.* **48**, 055501.

YAMAGAMI, T., SUZUKI, Y. & KASAGI, N. 2005 Development of feedback control system of wall turbulence using MEMS devices. In *Proceedings of 6th Symposium on Smart Control of Turbulence*, pp. 135–141.

YOSHINO, T., SUZUKI, Y. & KASAGI, N. 2008 Drag reduction of turbulence air channel flow with distributed micro sensors and actuators. *J. Fluid Sci. Technol.* **3**, 137–148.

YUN, J. & LEE, J. 2017 Prediction of near wall velocity in turbulent channel flow using wall pressure based on artificial neural network. In *Proceedings of the Korean Society of Mechanical Engineers Conference*, pp. 457–460. KSME.